The Middle to Late Miocene "Carbonate Crash" in the Equatorial Indian Ocean

メタデータ	言語: eng
	出版者:
	公開日: 2022-09-02
	キーワード (Ja):
	キーワード (En):
	作成者:
	メールアドレス:
	所属:
URL	https://doi.org/10.24517/00067012

The Middle to Late Miocene "Carbonate Crash" in the Equatorial Indian Ocean

Julia Lübbers[1] [iD], **Wolfgang Kuhnt[1]** [iD], **Ann E. Holbourn[1]** [iD], **Clara T. Bolton[2]** [iD], **Emmeline Gray[2]**, **Yoichi Usui[3]** [iD], **Karlos G. D. Kochhann[1,4]** [iD], **Sebastian Beil[1]** [iD], and **Nils Andersen[5]** [iD]

[1]Institute of Geosciences, Christian-Albrechts-University, Kiel, Germany, [2]CNRS, IRD, Collège de France, INRA, CEREGE, Aix-Marseille Université, Aix-en-Provence, France, [3]Department of Deep Earth Structure and Dynamics Research, Japan Agency for Marine-Earth Science and Technology, Kanagawa, Japan, [4]Geology Graduate Program, UNISINOS University, São Leopoldo, Brazil, [5]Leibniz Laboratory for Radiometric Dating and Stable Isotope Research, Christian-Albrechts-University, Kiel, Germany

Abstract We integrate benthic foraminiferal stable isotopes, X-ray fluorescence elemental ratios, and carbonate accumulation estimates in a continuous sedimentary archive recovered at International Ocean Discovery Program Site U1443 (Ninetyeast Ridge, Indian Ocean) to reconstruct changes in carbonate deposition and climate evolution over the interval 13.5 to 8.2 million years ago. Declining carbonate percentages together with a marked decrease in carbonate accumulation rates after ~13.2 Ma signal the onset of a prolonged episode of reduced carbonate deposition. This extended phase, which lasted until ~8.7 Ma, coincides with the middle to late Miocene carbonate crash, originally identified in the eastern equatorial Pacific Ocean and the Caribbean Sea. Interocean comparison reveals that intense carbonate impoverishment at Site U1443 (~11.5 to ~10 Ma) coincides with prolonged episodes of reduced carbonate deposition in all major tropical ocean basins. This implies that global changes in the intensity of chemical weathering and riverine input of calcium and carbonate ions into the ocean reservoir were instrumental in driving the carbonate crash. An increase in U1443 Log (Ba/Ti) together with a change in sediment color from red to green indicate a rise in organic export flux to the sea floor after ~11.2 Ma, which predates the global onset of the biogenic bloom. This early rise in export flux from biological production may have been linked to increased advection of nutrients and intensification of upper ocean mixing, associated with changes in the seasonality and intensity of the Indian Monsoon.

1. Introduction

During the middle to late Miocene, Earth's climate transitioned from a warmer phase with a reduced and highly dynamic Antarctic ice sheet to a colder, more permanently glaciated mode (Figure 1). This extended interval provides insights into different modes of natural climate variability on a warmer Earth, predominantly influenced by a Southern Hemisphere ice sheet. However, our understanding of underlying processes driving climate change following pulses of glacial expansion and global cooling at ~13.9 and ~13.1 Ma remains enigmatic, because sediment successions within the interval 13 to 8 Ma are often incomplete due to pervasive carbonate dissolution.

Earlier studies identified a distinctive seismic reflector in the tropical eastern and central Pacific Ocean, which was dated at 9.1 to 10.1 Ma. The reflector relates to a change in deposition from sediments with a predominantly high calcium carbonate content to an interval with high-amplitude fluctuations in carbonate content and increasing intercalations of silica-rich intervals (Mayer et al., 1985; Mayer et al., 1986). The interval, interpreted as an abrupt rise of the carbonate compensation depth (CCD) at ~10 Ma that lasted 2 to 3 million years in the tropical eastern Pacific Ocean, was termed the "carbonate crash" by Lyle et al. (1995). Intense carbonate dissolution episodes between 12 and 10 Ma were subsequently identified in the Caribbean Sea and linked to reorganization of the global ocean circulation system following initial closure of the Central American Seaway (Roth et al., 2000). Whereas most studies of the carbonate crash have focused on the eastern equatorial Pacific Ocean, its impact on oligotrophic regions of the global ocean remains contentious (e.g., Berger et al., 1993; Diester-Haass et al., 2004; Nathan & Leckie, 2009; Preiß-Daimler et al., 2013).
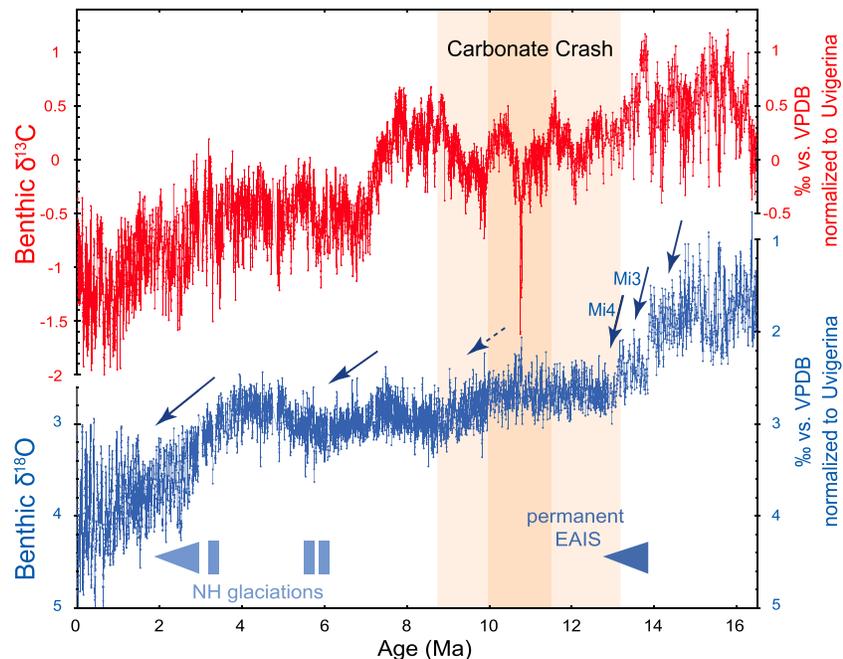
Figure 1. Miocene to Pleistocene (16–0 Ma) benthic foraminiferal $\delta^{18}O$ and $\delta^{13}C$ records from Ocean Drilling Program Site 1146. Orange shading marks interval targeted in this study; blue arrows mark main phases of glacial expansion/deepwater cooling. Modified from Holbourn et al. (2018) under license of Creative Commons Attribution 4.0 International License (https://creativecommons.org/licenses/by/4.0/). VPDB = Vienna PeeDee Belemnite.

A number of hypotheses have been put forward to explain the cause of the carbonate crash including: (1) enhanced primary production of siliceous and organic-walled phytoplankton in the equatorial Pacific high-productivity belt (Theyer et al., 1985) that may have led to degradation of organic carbon (C_{org}) in the water column and at the sea floor resulting in reduced alkalinity of intermediate deep and pore waters favoring carbonate dissolution (Archer, 1991; Emerson & Bender, 1981); (2) high-latitude cooling and expansion of polar ice caps that may have released C_{org} from exposed continental shelves during periods of major sea level fall (Barron et al., 1985); (3) changing trends in carbonate and silica deposition, caused by reduced deepwater exchange through the Central American Seaway and reorganization of the Atlantic and Pacific circulation toward modern patterns with a deeper CCD in the Atlantic Ocean (Farrell et al., 1995; Keller & Barron, 1983; Lyle et al., 1995); (4) northward expansion of corrosive southern-sourced intermediate and deepwater masses following the growth of the East Antarctic ice sheet during the middle to late Miocene that may have resulted in a CCD rise and increased carbonate dissolution in the Atlantic and Pacific Oceans (Preiß-Daimler et al., 2013); and (5) closure of the Indonesian Seaway that may have induced a reorganization in ocean circulation associated with major changes in equatorial productivity (Jiang et al., 2007). To date, however, the drivers of this prolonged episode of carbonate starvation in the eastern equatorial Pacific and Caribbean Sea remain unresolved.

The impact of the carbonate crash on the Indian Ocean, which is central to the interaction of different intermediate and deepwater masses, has thus far only been explored in relatively low-resolution studies (e.g., Peterson et al., 1992; Peterson & Backman, 1990). Continuous Miocene sedimentary archives from the Indian Ocean are scarce and existing stable isotope records spanning this extended interval are still poorly resolved. International Ocean Discovery Program Expedition 353 redrilled Ocean Drilling Program Site 758 on Ninetyeast Ridge in the southern Bay of Bengal with improved techniques and recovered a complete Miocene sediment succession at Site U1443 (Figure 2; Clemens et al., 2015). For this study, we integrated benthic foraminiferal stable oxygen and carbon isotope data, X-ray fluorescence (XRF) core scanner-derived elemental ratios and carbonate mass accumulation rates (MARs) from Site U1443 to closely track the development of the carbonate crash in the Indian Ocean and to investigate linkages with high-latitude climate evolution and with circulation changes in the Pacific and Atlantic Oceans.
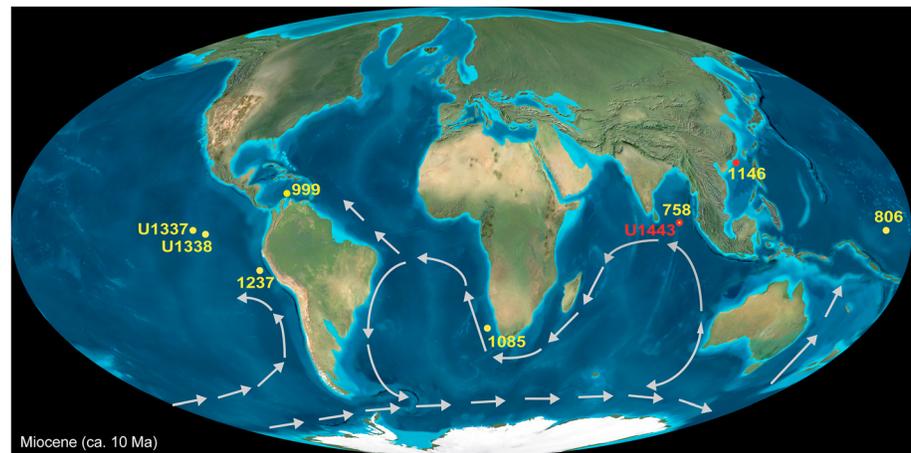
Figure 2. Late Miocene (10 Ma) paleogeography (Ron Blakey, Colorado Plateau Geosystems), intermediate/deepwater circulation pathways (gray arrows; Roth et al., 2000; Butzin et al., 2011) and locations of Ocean Drilling Program/ International Ocean Discovery Program sites (yellow dots) with records of the middle/late Miocene carbonate crash.

1.1. Oceanographic and Climatic Setting

Today, the equatorial Indian Ocean and surrounding landmasses are strongly influenced by seasonal changes in wind and precipitation associated with the Indian Monsoon. The generally dry northeasterly winds drive surface circulation counterclockwise in the Arabian Sea and Bay of Bengal during winter, whereas the wet southwesterly winds give rise to a clockwise circulation during summer. Consequently, there is a strong seasonal contrast between the freshwater export from the Bay of Bengal, which dominates during autumn and winter and the eastward transfer of saline and nutrient-rich waters from the Arabian Sea into the southern Bay of Bengal during summer (Gordon et al., 2016; Goswami et al., 2016). The transfer of nutrient-rich surface waters originating from the upwelling systems at the eastern margins of the Arabian Sea during the summer monsoon strongly impacts productivity as well as the amount and composition of the particle export flux to the deep sea in the southern Bay of Bengal (Unger et al., 2003; Unger & Jennerjahn, 2009). The ratio of particulate organic flux to primary production is unusually high in the Bay of Bengal (Gauns et al., 2005; Ittekkot et al., 1991; Lutz et al., 2002) due to ballasting by abundant riverine mineral particles, resulting in reduced decomposition rates of organic matter in the water column and at the sediment surface (Iversen & Ploug, 2010; Klaas & Archer, 2002; Le Moigne et al., 2013).

The present location of Site U1443 is bathed by Indian deep water (IDW), which extends into the equatorial and northern Indian Ocean at depths of 3,800 to ~1,500 m. IDW is characterized by relatively high salinity, reaching a maximum of 34.75 in the eastern Indian Ocean (Tomczak & Godfrey, 2003). Temperature, salinity, and oxygen properties of IDW are close to that of North Atlantic deep water in the Atlantic sector of the Southern Ocean, indicating that IDW is mainly derived from this water mass and is not primarily formed in the Southern Ocean (Tomczak & Godfrey, 2003). In contrast, Antarctic bottom water, which spreads below IDW at depths >3,800 m, has its source in the Southern Ocean (Tomczak & Godfrey, 2003). Thermocline waters in the Bay of Bengal consist of Indian Central Water originating from the Southern Hemisphere and of Indonesian throughflow water derived from North Pacific Intermediate Water, which is modified by intense mixing during transit through the Indonesian seas (Tomczak & Godfrey, 2003). During the Miocene, however, water mass characteristics may have substantially differed, as the wider and deeper Indonesian passage likely promoted a more intensified transfer of Pacific deep and intermediate waters into the Indian Ocean (Kuhnt et al., 2004).

2. Material and Methods

2.1. Sampling Strategy

Site U1443 was drilled on the crest of Ninetyeast Ridge (5°23.01′N, 90°21.7′E) at 2,925 m water depth (Figure 2). Based on new high-resolution XRF scanner elemental data and benthic isotope records, we

slightly modified the position of the original tie points defining the shipboard sediment splice in the middle to upper Miocene interval investigated in this study (supporting information Table S1). These modifications resulted in the overall addition of 12 cm to the meters composite depth (mcd) scale. The U1443 cores were sampled at 2 cm intervals (corresponding to ~3- to 8-kyr time resolution) along the revised splice from 113.4 to 140.2 mcd. The depth interval corresponds to ~13.5 to ~8 Ma, based on the shipboard preliminary age model. The sediment consists of calcareous nannofossil ooze with foraminiferal tests and minor amounts of clay, siliceous microfossils, and volcanic ash. Detailed sedimentologic descriptions and physical properties are provided by Clemens et al. (2016).

2.2. Stable Isotope Analysis

Micropaleontological samples were oven dried at 40 °C, weighed and washed over a 63 μm sieve. The residues were oven dried at 40 °C, then weighed and sieved in different size fractions. We picked four to six specimens of the epifaunal foraminifera *Cibicidoides wuellerstorfi* from the size fractions >250 μm for stable isotope analysis. Tests were broken into fragments, cleaned in ethanol in an ultrasonic bath and oven dried at 40 °C. Stable carbon and oxygen isotopes were measured with a Finnigan-MAT 253 mass spectrometer at the Leibniz Laboratory, University of Kiel. The instrument is coupled online to a Carbo-Kiel Device (Type IV) for automated CO_2 preparation from carbonate samples for isotopic analysis. Samples were reacted by individual acid addition (99% H_3PO_4 at 75 °C). Replicate measurements of samples indicate mean reproducibility better than ±0.09‰ for $\delta^{18}O$ and $\delta^{13}C$. Results were calibrated using the National Institute of Standard and Technology (Gaithersburg, MD) carbonate isotope standard National Bureau of Standard 19 and the international carbonate standard International Atomic Energy Agency 603 and are reported on the Vienna PeeDee Belemnite scale.

2.3. Age Model

We analyzed an additional 17 samples from the splice for nannofossil biostratigraphy to increase the depth resolution of the three uppermost nannofossil datums to less than ±0.5 m (relative to shipboard data, where these events were only defined to within ±1.5 m or ±2.4 m) and to verify the depths of these events in splice samples from which we generated XRF and isotope data. This led to the revision of the three youngest nannofossil datums. Nannofossil datums in the older part of the study interval (>10 Ma), as well as planktonic foraminiferal datums, were not further refined. Age assignments for all datums were not altered relative to those used in the shipboard biostratigraphy (Clemens et al., 2015).

We also revised the shipboard paleomagnetic data (Clemens et al., 2015). Paleomagnetic polarities were estimated by alternating field demagnetization of u-channel samples covering the interval. Because inclination is generally small, we mainly used declination to assign polarity zones. The interval below 130 mcd matches well with the Global Magnetic Polarity Timescale 2012 (Ogg, 2012). However, multiple polarity reversals above 130 mcd, which coincide with the up-core transition from stronger to weaker remanence, are not interpretable.

We then refined the Site U1443 age model by correlating our new benthic $\delta^{18}O$ and $\delta^{13}C$ records to the astronomically tuned record of Ocean Drilling Program Site 1146 using a minimal tuning approach (e.g., Holbourn et al., 2013; Holbourn et al., 2018) between 13.5 and 8.2 Ma (Table 1 and supporting information Figures S1 and S2). Tuning was performed with AnalySeries 2.0.8. (Paillard et al., 1996).

2.4. Spectrophotometry

During Expedition 353, reflectance of visible light was measured on the archive halves of freshly split sediment cores using an Ocean Optics USB4000 spectrophotometer with a diffuse light source mounted on an automated multisensor logger. The cores were covered with clear plastic wrap, and measurements with a circular footprint of 8 mm were taken at 2.5 cm spacing for the spectral band between 400 and 900 nm (Clemens et al., 2015). We use the lightness (L*) value as an indicator of carbonate content (supporting information Figure S3c; e.g., Balsam et al., 1999; Giosan et al., 2002) and the red/green (a*) value as an indicator of the relative contribution of clay to the sediment. The deposition of red clays occurs mainly in distal regions of the oceans, where primary production, organic export flux, and sedimentation rates are low and where pore waters remain oxic (Glasby, 1991). Under a high primary production and export flux regime, oxygen is rapidly consumed in the sediment due to the elevated rates of organic carbon remineralization and reducing pore waters. These conditions lead to rapid reduction of brown oxidized (ferric, Fe-III) iron at the

Table 1
Biostratigraphy Datums, Magnetostratigraphy, and Tie Points Used to Derive Site U1443 Age Model

(a) Calcareous Nannofossil Datums, Site U1443

	Top	Bottom	Midpoint depth (mcd)	GTS2012 age (Ma)	Tuned age (Ma)
B Discoaster berggrenii	U1443C-13H5W, 60–61 cm	U1443B-12H2W, 3–4 cm	113.04 ± 0.36	8.29	8.18
T Discoaster hamatus	U1443B-13H3W, 2–3 cm	U1443A-13H3W, 15 cm	125.70 ± 0.20	9.53	9.46
B Discoaster brouweri	U1443A-13H4W, 15 cm	U1443A-13H5W, 15 cm	128.15 ± 0.75	10.76	10
B Catinaster coalitus	U1443A-13H5W, 15 cm	U1443A-13H6W, 15 cm	129.65 ± 0.75	10.89	10.34
T Coccolithus miopelagicus	U1443A-13H7W, 15 cm	U1443A-13HCC	132.30 ± 0.40	10.97	11.02
Bc Discoaster kugleri	U1443A-14H1W, 15 cm	U1443A-14H2W, 15 cm	134.39 ± 0.75	11.9	11.81
T Coronocyclus nitescens	U1443A-14H1W, 15 cm	U1443A-14H2W, 15 cm	134.39 ± 0.75	12.12	11.81
B Triquetrorhabdulus rugosus	U1443A-14H2W, 15 cm	U1443A-14H2W, 15 cm	135.89 ± 0.75	13.27	12.36

(b) Planktic Foraminiferal Datums, Site U1443

	Top	Bottom	Midpoint depth (mcd)	GTS2012 age (Ma)	Tuned age (Ma)
B Globigerinoides extremus	U1443A-11HCC	U1443A-12HCC	116.67 ± 4.82	8.93	8.42
B Neogloboquadrina acostaensis	U1443A-12HCC	U1443A-13HCC	127.76 ± 4.93	9.83	9.92
T Paragloborotalia mayeri/siakensis	U1443A-12HCC	U1443A-13HCC	127.76 ± 4.94	10.46	9.92
T Fohsella fohsi, Fohsella plexus	U1443A-13HCC	U1443A-14HCC	138.55 ± 4.62	11.79	13.21

(c) Magnetostratigraphy, Site U1443

Chron Name	Chron top depth (mcd)	Chron top GTS2012 age (Ma)	Tuned age (Ma)
C5n.2n	129.25	9.98	10.25
C5r.1r	133.77	11.06	11.57
C5r.2n	134.38	11.59	11.8
C5r.3r	134.66	11.66	11.91
C5An.1n	135.18	12.05	12.11
C5An.1r	136.15	12.17	12.1
C5An.2n	136.30	12.27	12.5
C5Ar.1r	136.92	12.47	12.72
C5AAn	137.67	13.03	12.98
C5AAr	138.42	13.18	13.19

(d) Tie Points, Site U1443

Description	Tie point	Depth (mcd)	Age (Ma)
$\delta^{13}C$ Maximum (1.18‰)	U1443B-12H5W, 28–29 cm	118.14	8.51
$\delta^{13}C$ Minimum (0.58‰)	U1443C-15H3W, 94–95 cm	120.72	8.68
$\delta^{13}C$ Minimum (0.55‰)	U1443C-15H5W, 16–17 cm	122.95	9.01
$\delta^{13}C$ Minimum (0.41‰)	U1443B-13H3W, 8–9 cm	125.55	9.43
Warm Event: $\delta^{18}O$ Minimum (1.99‰) and $\delta^{13}C$ Minimum (0.4‰)	U1443C-16H4W, 66–67 cm	131.65	10.78
$\delta^{13}C$ Maximum (1.11‰)	U1443C-16H5W, 135–136 cm	133.84	11.60
$\delta^{13}C$ Minimum (0.46‰)	U1443B-14H2W, 35–36 cm	135.12	12.09
$\delta^{18}O$ Minimum (1.99‰)	U1443B-14H4W, 35–36 cm	138.12	13.14
$\delta^{18}O$ Minimum (1.97‰) and $\delta^{13}C$ Minimum (0.96‰)	U1443B-14H5W, 48–49 cm	139.75	13.42

Note. (a–c) Revised and shipboard calcareous nannofossil datums, shipboard planktonic foraminifer datums, and revised magnetostratigraphy; (d) Age tie points used for correlation of Sites U1443 and 1146. Mcd = meters composite depth, B = bottom (first occurrence), T = top (last occurrence), Bc = bottom common, GTS2012 = Geologic Timescale 2012 (Gradstein et al., 2012).

sediment surface to reduced gray-green or green ferrous (Fe-II) iron minerals (König et al., 1997; Lyle, 1983). In contrast, at sites with low rates of organic matter deposition and sedimentation rates, diffusion of oxygen into the sediment column exceeds consumption through organic matter oxidation. Thus, iron minerals remain in the ferric (Fe-III) state and sediment colors remain grayish-brownish-reddish.

2.5. XRF Core Scanning

Elemental composition was analyzed using a second generation Avaatech XRF core scanner at the Institute of Geosciences at the University of Kiel. XRF scanner data were collected along the shipboard splice from Core 1443B-12H-2 (113.37 mcd) to Core U1443B-14H-5 (140.2 mcd) with approximately 1m overlaps at the splice tie points. Measurements were taken every 1 cm over a 1.2 cm^2 area with a downcore slit size of 10 mm and a crosscore slit of 12 mm, using generator settings of 10 kV (10 s acquisition time, 750 μA, and without filter) and 50 kV (20 s acquisition time, 2,000 μA, and Cu filter). The archive core sections were covered with a 4-μm thin Chemplex Prolene Thin-Film foil to avoid contamination of the XRF detector. Data were acquired using the XR-100CR detector from Amptek and the Oxford Instrument 50W XTF5011 X-Ray tube with rhodium (Rh) target material. Raw X-ray spectra were processed with the iterative least square software package WIN_AXIL from Canberra Eurisys. Results are reported as logarithms of elemental ratios, which provide the most easily interpretable signals of relative changes in chemical composition and minimize the risk of measurement artefacts from variable signal intensities and matrix effects (Weltje & Tjallingii, 2008).

We used the logarithmic ratio of calcium (Ca) to the sum of the terrigenous elements (Al, K, Ti, Fe, and Si), which we refer to as Log (Ca/Terr.), to estimate changes in the relative contribution of carbonate and clay to the sediment (supporting information Figure S4a). We assumed that terrigenous input (aeolian dust or river runoff) remained relatively steady at this distal location and that past carbonate production, export flux and dissolution mainly control Log (Ca/Terr.). This assumption is supported by the nearly constant sediment flux between 15 and 9 Ma in this part of the Indian Ocean (McNeill et al., 2017). We also used the Log (Al/Ti) to evaluate changes in sediment transport mechanisms from source to sink and to assess the contribution of wind-blown dust to the terrigenous component (supporting information Figure S4e).

We used Log (Ba/Al) and Log (Ba/Ti) as indicators of paleoproductivity and organic export flux (supporting information Figures S4b and S4d). Goldberg and Arrhenius (1958) originally suggested that the accumulation rate of barium in deep-sea sediments is a function of the rate of organic production in the euphotic zone and used BaO/TiO_2 to trace the zone of upwelling-related enhanced productivity in the equatorial Pacific Ocean. Total Ba, as measured by the XRF core scanner, closely matches biogenic Ba in deep marine sedimentary environments, which do not contain Ba from terrigenous sources and where no significant barite remobilization occurs (Dymond et al., 1992; Hendy, 2010; Horner et al., 2017; Piela et al., 2012; Torres et al., 1996; Von Breymann et al., 1992). The dissolution resistance of biogenic barium and its strong correlation with the organic carbon (C_{org}) export flux additionally make Ba/Al a robust indicator of C_{org} export flux in sediments with low clay content (Dymond et al., 1992; Eagle et al., 2003; Piela et al., 2012). We normalized XRF scanner Ba counts against Ti and Al, considered representative of the relatively constant clay flux over the 13.5 to 9 Ma interval (McNeill et al., 2017).

2.6. Calibration of XRF-Derived Carbonate Content

The carbonate content of 58 discrete samples was measured at a resolution of ~1 m in order to calibrate the U1443 XRF scanner Ca data. Total carbon (TC) was measured with a Carlo Erba Elemental Analyzer at the Helmholtz Centre for Ocean Research in Kiel (Geomar). Measurements were duplicated and averages are presented. As the total organic carbon (TOC) concentration was extremely low, a mean of 0.1% was used to calculate carbonate concentration (Clemens et al., 2015). To calculate the calcium carbonate ($CaCO_3$) concentration, we used the equation:

$$CaCO_3 = [TC\ (\%) - TOC\ (\%)]^* 8.3333\ (Verardo\ et\ al.,\ 1990).$$

Discrete measurements were plotted against the ratio of XRF scanner Ca area counts (in counts per second) versus the sum of Ca, Al, Si, K, Ti, Mn, Fe and S area counts, following Lyle and Backman (2013). Linear regression enabled us to calibrate the XRF-derived (Ca/$\sum$(Ca, Al, Si, K, Ti, Mn, Fe, S)) into $CaCO_3$ concentrations. Deviations between discrete $CaCO_3$ measurements and XRF estimated $CaCO_3$ concentrations due to porosity changes with depth are negligible, because little change in porosity occurs over the interval of interest. Shipboard moisture and density measurements on discrete samples indicate a narrow porosity range between 66.7% and 58.9% (stdev 1.9%, $n = 17$) without any downcore trend. This

method varies from the method of Lyle and Backman (2013), since we only measured the carbonate content and not the complete elemental composition of the bulk sediment. Discrete $CaCO_3$ measurements show only minor deviations from XRF estimated $CaCO_3$ concentrations (supporting information Figure S3d). The linear regression between the discrete measurements and (Ca/$\sum$(Ca, Al, Si, K, Ti, Mn, Fe, S)) has an R^2 of 0.81 ($n = 58$), which is comparable with the result ($R^2 = 0.87$, $n = 255$) of Lyle and Backman (2013).

2.7. Carbonate Mass Accumulation Rates

Carbonate mass accumulation rates ($MAR_{carbonate}$; g cm^{-2} kyr^{-1}) are based on the carbonate contents (%), linear sedimentation rates (LSRs; cm/kyr), and dry bulk densities (g/cm^3). LSRs were interpolated between age control tie points using a 5% locally weighted least squared error (Lowess) fit. Dry bulk densities (DBD) were linearly interpolated from shipboard gamma ray attenuation (GRA) bulk densities, after converting GRA bulk densities to dry bulk densities according to the linear relationship DBD = 1.215 + 1.3164 GRA; $R^2 = 0.77$ (e.g., Pälike et al., 2010). To calculated $MAR_{bulk\ sediment}$ (g cm^{-2} kyr^{-1}), we multiplied LSRs and dry bulk densities. To calculate $MAR_{carbonate}$, we used the following equation:

$$MAR_{carbonate} = (CaCO_3\%/100)^* \ MAR_{bulk\ sediment}.$$

2.8. Benthic/Planktic Foraminiferal Ratios

Benthic/Planktic (B/P) foraminiferal ratios were determined in 394 samples by counting ~300 complete specimens per sample and are reported as percentages B/(B+P)*100 (Van der Zwaan et al., 1990). In samples with fewer than 300 individuals, we counted all foraminifers. We interpret the B/P ratio mainly as an indicator of carbonate dissolution, since planktic foraminiferal tests are generally thin walled and more susceptible to dissolution than robust thick-walled benthic foraminifers. In a statistical analysis of the reliability of carbonate dissolution indices in Pleistocene deep-sea cores, the "dissolution" principal component explains more than 68% of the variance for the B/P ratio (Thunnell, 1976). These early results were corroborated by more recent studies using experimental dissolution of fossil benthic and planktic foraminifers (Boltovskoy & Totah, 1992; Nguyen et al., 2009). We are aware that this ratio also depends on the food supply to benthic foraminifers and, thus, is influenced by changes in the export production flux (e.g., Berger & Diester-Haass, 1988).

2.9. Light Microscope and Scanning Electron Microscope (SEM) Analysis of Dissolution Effects on Foraminiferal Assemblages

Five samples from Site U1443 were selected based on their different carbonate contents in order to assess foraminiferal preservation. We examined the planktonic foraminifer *Trilobatus sacculifer* or *Sphaeroidinellopsis disjuncta* (when *T. sacculifer* was absent during the low-carbonate phase) and the benthic species *Cibicidoides wuellerstorfi* for signs of dissolution in each of these samples. The foraminifers were mounted onto SEM stubs, sputter coated with gold/palladium and their state of preservation was examined with a CamScan 44 SEM.

3. Results

3.1. Chronology

Comparison of the benthic stable isotope records from Site 1146 (South China Sea), representative of the subtropical Northwest Pacific (Holbourn et al., 2013), and from Site U1443 (equatorial Indian Ocean) between 13.5 and 8.2 Ma reveals similar long- and short-term trends even on a relatively fine orbital scale, which allows detailed correlation of the records (Figures 3, 4, and S1). Correlation of the $\delta^{18}O$ and $\delta^{13}C$ records from these sites is based on nine tie points (Figures 3, 4, and S1 and Table 1d). We used the $\delta^{18}O$ minimum at the onset of the peak warm event at 10.7 Ma as a primary tie point, supplemented by four $\delta^{13}C$, two $\delta^{18}O$ minima and two $\delta^{13}C$ maxima, which are distinctive in both records. The resulting mean sedimentation rate at Site U1443 is ~0.61 cm/kyr for the 13.5 to 8.2 Ma interval with a maximum of ~1.55 cm/kyr between 8.7 and 8.2 Ma and a minimum of ~0.26 cm/kyr between 13.1 and 10.8 Ma (Figure 4a). A stepwise increase in sedimentation rates from 0.26 to 0.65 cm/kyr occurs between 10.8 and 8.7 Ma, followed by a marked rise
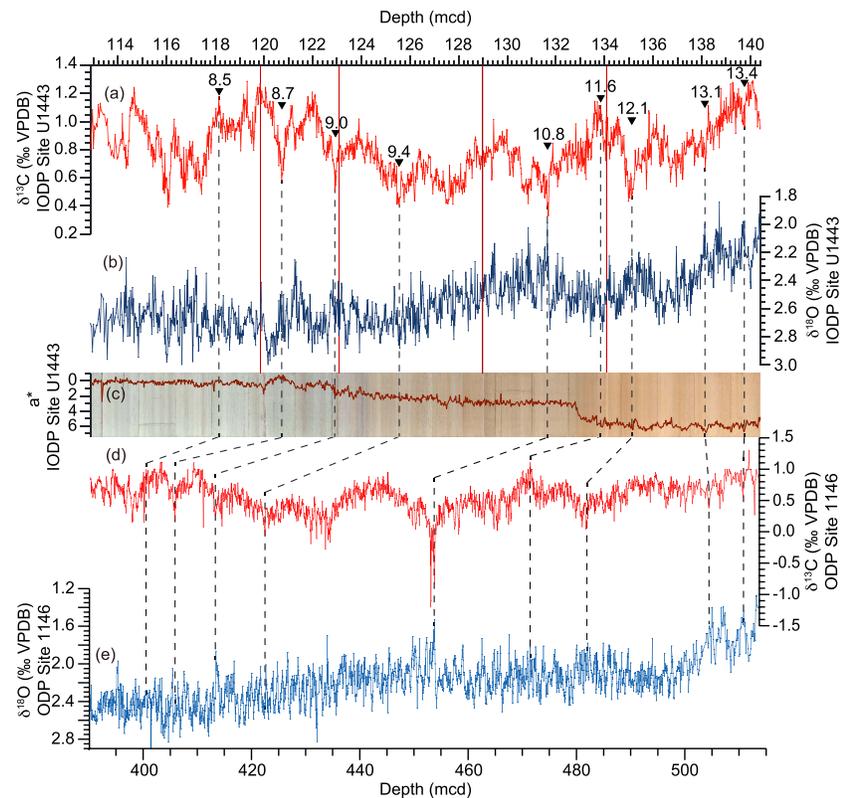
Figure 3. Correlation of benthic foraminiferal $\delta^{18}O$ and $\delta^{13}C$ records from Indian Ocean Site U1443 and South China Sea Site 1146. (a) Benthic foraminiferal $\delta^{13}C$ from Site U1443; (b) benthic foraminiferal $\delta^{18}O$ from Site U1443; (c) color reflectance (a*) record from Site U1443 (Clemens et al., 2015), plotted on composite core image of the splice; (d) benthic foraminiferal $\delta^{13}C$ from Site 1146 (Holbourn et al., 2018); and (e) benthic foraminiferal $\delta^{18}O$ from Site 1146 (Holbourn et al., 2018). Correlation tie points (Ma) based on benthic stable isotope records between Ocean Drilling Program Site 1146 and International Ocean Discovery Program Site U1443 are indicated by black arrows and dashed lines. Site U1443 splice tie points are indicated by red lines.

from 0.65 to 1.55 cm/kyr at 8.7 Ma (Figure 4a). The average chronological resolution for stable isotope measurements between 13.5 and 8.2 Ma varies between ~3 and ~8 kyr.

3.2. Temporal Evolution of Benthic $\delta^{18}O$ and $\delta^{13}C$

The U1443 stable isotope data are plotted against composite depth in Figure 3 and against age in Figure 4. Between 13.5 and 8.2 Ma, benthic $\delta^{18}O$ varies between 1.8‰ and 3.1‰ with a mean of 2.6‰ and standard deviation of 0.19‰ (Figure 4b). The $\delta^{18}O$ curve displays a distinct step between 13.2 and 13.0 Ma, followed by a long-term increasing trend of ~0.5‰ (400 kyr running mean; Figure 4b). A distinctive feature of the $\delta^{18}O$ record is the abrupt decrease of ~0.7‰, which marks the onset of a transient warming episode at ~10.8–10.7 Ma, previously identified at Site 1146 in the South China Sea (Figure 4c; Holbourn et al., 2013). At both sites, the $\delta^{18}O$ minimum coincides with a negative $\delta^{13}C$ excursion (Figure 4). Between 13.5 and 8.2 Ma, benthic $\delta^{13}C$ at Site U1443 generally fluctuates between 1.3‰ and 0.3‰ with a mean of 0.8‰ and standard deviation of 0.19‰ (Figure 4d). The U1443 $\delta^{13}C$ curve displays low frequency fluctuations that approximate the ~400 kyr long eccentricity cycle and correlate with long-term variations in the 1146 $\delta^{13}C$ record (Figures 4d and 4e).

3.3. Carbonate Concentrations and Mass Accumulation Rates

Between ~13.5 and 8.2 Ma, the XRF scanner-derived $CaCO_3$ content at Site U1443 fluctuates between 87% and 43% (Figure 5a). From ~13.5 to 12.3 Ma, the $CaCO_3$ content remains relatively high, oscillating between 86% and 75%. A sharp drop to 68% at ~12.2 Ma marks the onset of a prolonged interval with highly variable
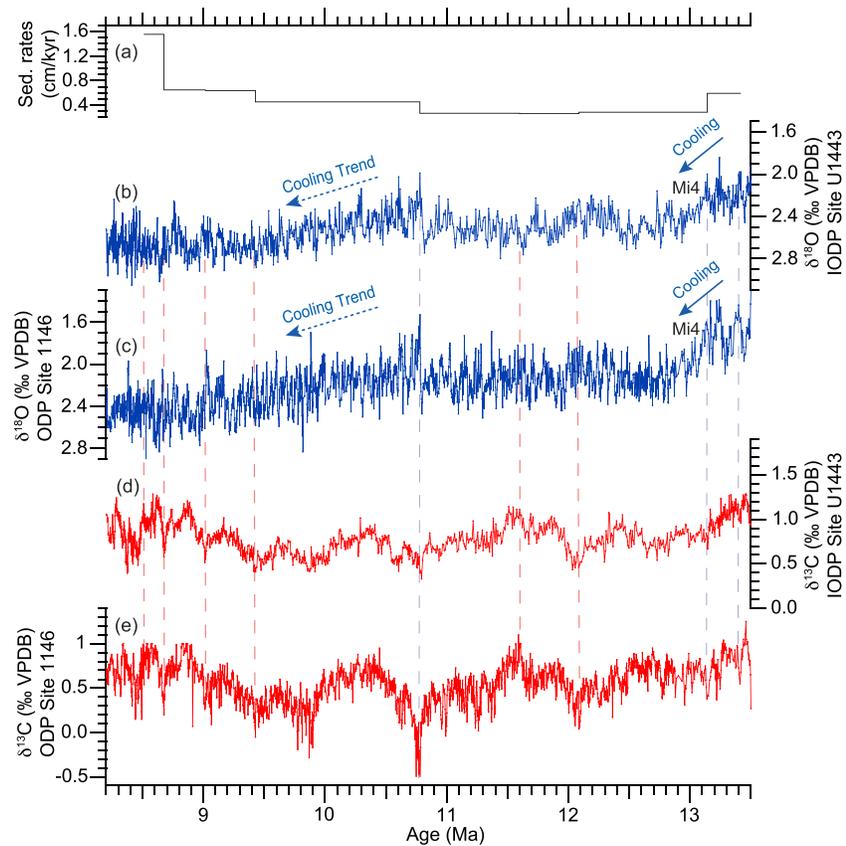
Figure 4. Age model, based on minimal tuning of U1443 and 1146 benthic foraminiferal $\delta^{18}O$ and $\delta^{13}C$ records. (a) Sedimentation (Sed.) rates (cm/kyr); (b) benthic foraminiferal $\delta^{18}O$ from Site U1443; (c) benthic foraminiferal $\delta^{18}O$ from Site 1146 (Holbourn et al., 2018); (d) benthic foraminiferal $\delta^{13}C$ from Site U1443; and (e) benthic foraminiferal $\delta^{13}C$ from Site 1146 (Holbourn et al., 2018). Tie points based on correlation of $\delta^{13}C$ are indicated by red dashed lines; tie points based on correlation of $\delta^{18}O$ are indicated by blue dashed lines. IODP = International Ocean Discovery Program; ODP = Ocean Drilling Program; VPDB = Vienna PeeDee Belemnite.

and generally lower CaCO₃ content (mainly below 70% with a minimum of 43% at ~10.2 Ma), which lasted until ~10.2 Ma. After ~10.2 Ma, the CaCO₃ record exhibits a long-term increasing trend, reaching ~84% at ~8.6 Ma. This increasing trend is only interrupted by three transient decreases between ~8.8 and 8.6 Ma, when values temporarily drop down to ~70%–60%. From 8.6 to 8.2 Ma, the CaCO₃ content remains high, generally varying between 87% and 82%.

The U1443 carbonate MAR record exhibits a distinct decrease from 0.5 to 0.2 g cm^{-2} kyr^{-1} at ~13.2 Ma, marking the onset of a prolonged interval with sustained low MARs (~0.2−0.3 g cm^{-2} kyr^{-1}), which lasted until ~10.2 Ma (Figure 5b). After ~10.2 Ma, MARs show a slight increasing trend, reaching 0.5 g cm^{-2} kyr^{-1} at ~8.7 Ma. This long-term increase is followed by a sharp rise from 0.5 to 1.3 g cm^{-2} kyr^{-1}. From 8.6 to 8.2 Ma, MARs generally hover between 0.4 and 0.3 g cm^{-2} kyr^{-1}.

Based on the carbonate content (% and MARs), we identify three distinct stages in the evolution of carbonate deposition at Site U1443 (Figure 5). (1) A slight declining trend in carbonate content together with a distinct decrease in MARs starting at ~13.2 Ma mark the initial phase, which lasted until ~12.2 Ma. The decrease in MARs at ~13.2 Ma is more abrupt than the decrease in carbonate %, which may partly be due to the linear interpolation between age tie points. (2) Between ~12.2 and ~10 Ma, our records reveal a highly fluctuating and generally lower carbonate contents, which together with sustained low MARs suggest more intense carbonate impoverishment at the sea floor. Minimum values in carbonate contents (43%) and lowest MARs (0.14 g cm^{-2} kyr^{-1}) are recorded within this interval. (3) Between ~10.2 and ~8.7 Ma, long-term rises in both carbonate contents and MARs signal a protracted recovery from the intense phase of reduced carbonate deposition.
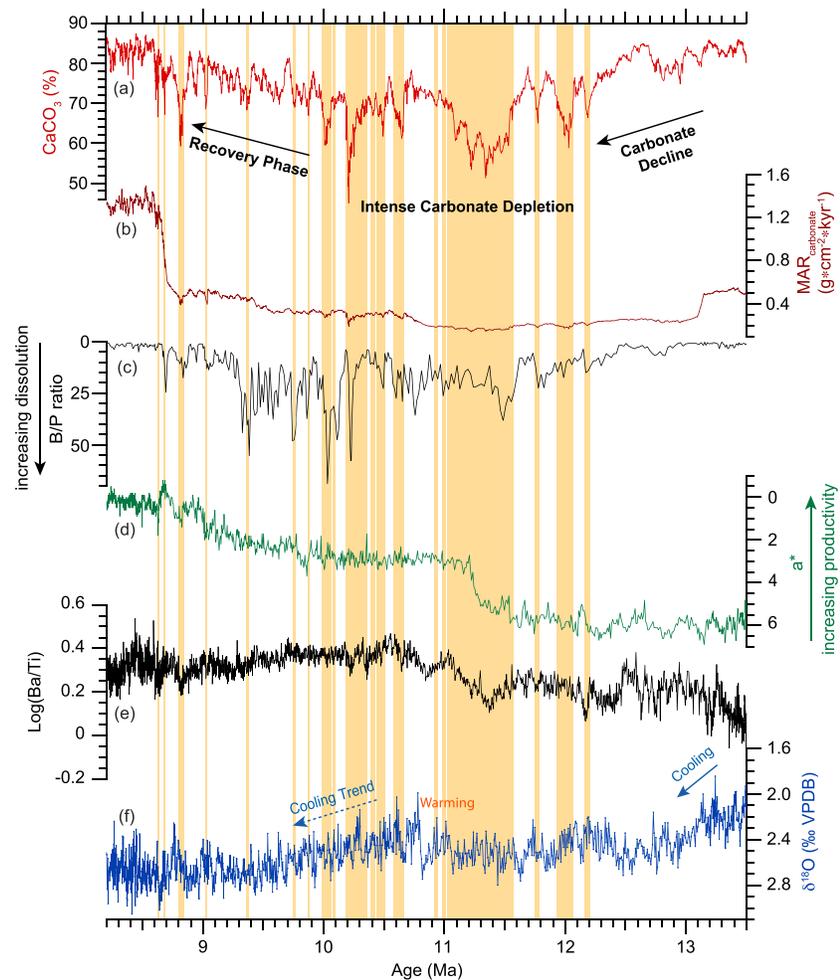
Figure 5. Paleoceanographic records at Site U1443. (a) XRF scanner-derived $CaCO_3$ (%); (b) Carbonate mass accumulation rate (g cm^{-2} kyr^{-1}); (c) Benthic/Planktonic foraminiferal ratio; (d) Color reflectance a* (Clemens et al., 2015); and (e) XRF scanner Log (Ba/Ti); (f) Benthic foraminiferal $\delta^{18}O$. Orange shading marks carbonate content under 70%. MAR = mass accumulation rate; VPDB = Vienna PeeDee Belemnite.

3.4. Evaluation of Carbonate Dissolution in Foraminiferal Assemblages

Examination of foraminiferal assemblages under the SEM and light microscope as well as assessment of benthic/planktic ratios and sediment coarse fraction percentages support that dissolution was more intense between ~13.2 and 8.7 Ma. In samples before and after this time interval, foraminiferal assemblages are well preserved, showing no evidence of carbonate dissolution (Figure 6) and benthic foraminifers comprise <1% of the assemblages, which is typical for deep-sea settings (Berger & Diester-Haass, 1988). In contrast, foraminiferal assemblages within the intense phase of carbonate impoverishment exhibit moderate to strong dissolution and benthic percentages increase markedly (Figures 5a and 5c). High benthic percentages (>25%, reaching peak values of >50%, Figure 5c) between ~10.2 and 9.4 Ma indicate that carbonate dissolution was intense at the onset of the recovery phase. However, enhanced export production, resulting in higher food supply at the sea floor, may also have contributed to the higher abundance of benthic foraminifers in this interval. Detailed descriptions of the five samples spanning and including the interval of low carbonate accumulation are provided in the supporting information.

3.5. Changes in XRF-Derived Indicators of Paleoproductivity

Log (Ba/Ti) show a slightly increasing trend from ~0.1 to ~0.3 between ~13.5 and 12.5 Ma, followed by a slight decrease at ~12.5 Ma. Values fluctuate around 0.2 from ~12.5 to 11.4 Ma (Figures 5e and S4d). A
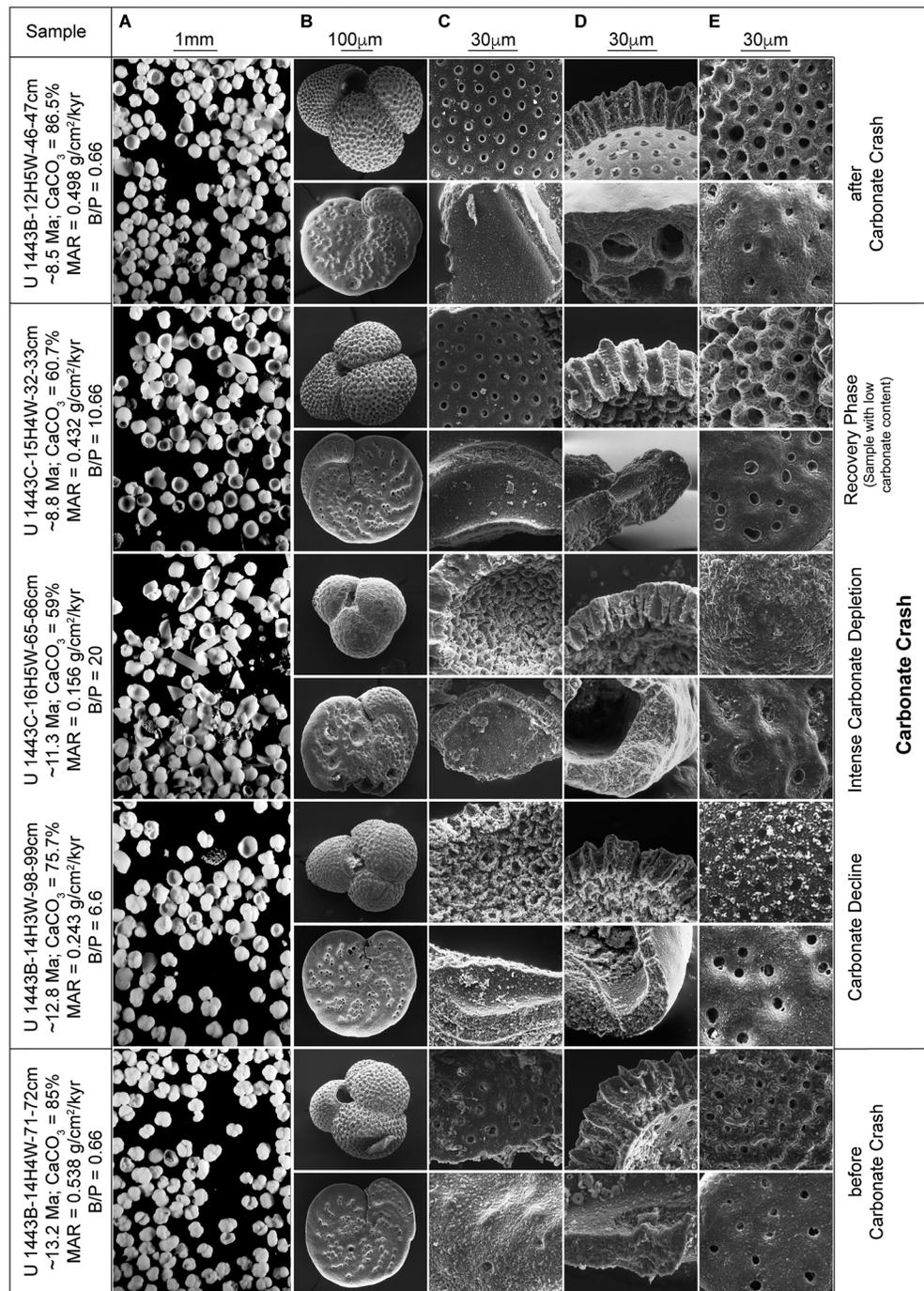
Figure 6. Foraminiferal preservation states at Site U1443. (a) Light microscope images of foraminiferal assemblage; (b) scanning electron microscope images of *Trilobatus sacculifer* (*Sphaeroidinellopsis disjuncta* in low carbonate interval due to absence of *T. sacculifer*) and *Cibicidoides wuellerstorfi*; (c–e) High-magnification images of (c) inner wall surfaces, (d) wall cross sections, and (e) outer wall surfaces.

stepwise increase in Log (Ba/Ti) from ~0.2 to ~0.4 occurs from ~11.4 to 10.6 Ma (Figures 5e and S4d), after which both log ratios oscillate around a mean of 0.3. Log (Ba/Al), Log (Ba/Si) and (Ba/Fe) display similar trends as Log (Ba/Ti) (supporting information Figures S6a–S6e). However, the amplitude of the changes is higher, when normalizing Ba against light elements (Log (Ba/Al) and Log (Ba/Si)) and lower when normalizing against heavier elements (Log (Ba/Ti) and Log (Ba/Fe)), suggesting that these log ratios are

affected by changes in the density composition of the terrigenous component, dependent on transport pathways.

3.6. Changes in Sediment Color to Evaluate Redox Conditions

A distinct decrease in color reflectance red-green (a*) values from 5.1 to 2.7 at ~11.3–11.2 Ma indicates a change in sediment color from reddish to gray (Figure 5d). Since sedimentation rates are constant over this interval, this change in sediment color indicates increased iron reduction by more oxygen depleted pore waters due to elevated organic export flux to the sea floor. A further gradual decrease in a* values to 0 occurs between ~9.8 and 8.7 Ma, after which values oscillate around 0 until 8.2 Ma, marking a further increase in iron reduction in pore waters.

4. Discussion

4.1. Evolution of Carbonate Crash in Atlantic, Pacific, and Indian Oceans

4.1.1. Diachronous Onset of Carbonate Crash

The middle to late Miocene carbonate crash has been mostly discussed from tropical locations in the eastern Pacific Ocean; additional hints that it may be more than a regional phenomenon come from sites in the Caribbean Sea and Indian Ocean (Figure 2 and supporting information Table S2). Moreover, if more widespread, the onset and initial decline phase of the carbonate crash in these basins remain uncertain. At Site U1443, a distinct decrease in carbonate MARs occurs at ~13.2 Ma and carbonate contents fall below 70% at ~12.2 Ma, marking the onset of the carbonate crash in the Indian Ocean (Figure 5). In contrast, carbonate contents and MARs at the Caribbean Site 999 and the eastern Pacific Sites U1338 and U1337 exhibit only slight decreasing trends and transient episodes of carbonate reduction prior to ~11.5 Ma (Figures 7b, 7d, and 7e and 8b–8d; Roth et al., 2000; Shackford et al., 2014; Lyle & Baldauf, 2015). At Site U1338, the starting point for the carbonate crash is poorly reflected in carbonate contents and MARs but was defined at 13.2 Ma by an increase in the number of diatom frustules (Lyle & Baldauf, 2015).

4.1.2. Global Extent of Deep-Sea Carbonate Impoverishment (~11.5 and 10 Ma)

At Site U1443, the most intense phase of the carbonate crash starts at ~12.2 Ma and the lowest carbonate contents (~80% to <50%, Figure 7a) and MARs (~0.18–0.34 g cm^{-2} kyr^{-1}, Figure 8a) occur between ~11.5 and 10 Ma. These low contents and MARs are comparable to those from abyssal Site U1337 in the equatorial eastern Pacific and from Site 999 and neighboring sites in the Caribbean Sea (Roth et al., 2000) over this interval (Figures 7b and 7e and 8b and 8d). However, they are generally lower than at eastern equatorial Pacific Site U1338 and at southeastern Pacific Site 1237 (Lyle et al., 1995; Lyle & Baldauf, 2015; Figures 8c and 8e). The higher carbonate MARs at Site U1338 may reflect its location near the Equator, where modern carbonate values on the sea floor are higher because of equatorial upwelling (Dunne et al., 2012). Interocean comparison shows that intense carbonate impoverishment at Site U1443 coincides with prolonged episodes of reduced carbonate deposition at low-latitude locations in other basins (Figures 7 and 8).

4.1.3. Regional Differences in the Recovery Phase (~10 to 8.5 Ma)

At ~10 Ma, the shallower Sites U1443, 999, and 1237 in the Indian Ocean, Caribbean Sea, and Southeast Pacific Ocean started to recover (Figures 7a, 7b, and 7f and 8a, 8b, and 8e), whereas carbonate % and MARs only began to increase after ~9.5 Ma at the deeper eastern equatorial Pacific Sites U1337 and U1338 (Figures 7d and 7e and 8c and 8d). Carbonate contents also remained low (~40%) at Site 1085 in the southeast Atlantic (Figure 7c). However, carbonate contents at this site, proximal to land, appear to be strongly influenced by siliciclastic dilution from the Oranje River (Diester-Haass et al., 2004).

Differences between age models for Sites U1337, U1338, and U1443 may introduce some discrepancies in the timing of events, but differences in the recovery phase from the carbonate crash may also relate to depositional environments and productivity regimes at the locations. Site U1337, which exhibits the most delayed recovery, is located on deeply subsided oceanic crust (Pälike et al., 2012). This abyssal site drifted northwest and away from the region of intense equatorial upwelling during the late Miocene and remained close to or even below the CCD from ~11.5 to 8.7 Ma. Site U1338 also migrated northwest during the late Miocene but was located in slightly shallower backtracked water depths and passed beneath the Equator at ~11 Ma (Pälike et al., 2010). In contrast to both these locations, Site U1443 remained beneath a more oligotrophic region and well above the regional CCD through the late Miocene. At all sites, the end of the carbonate crash
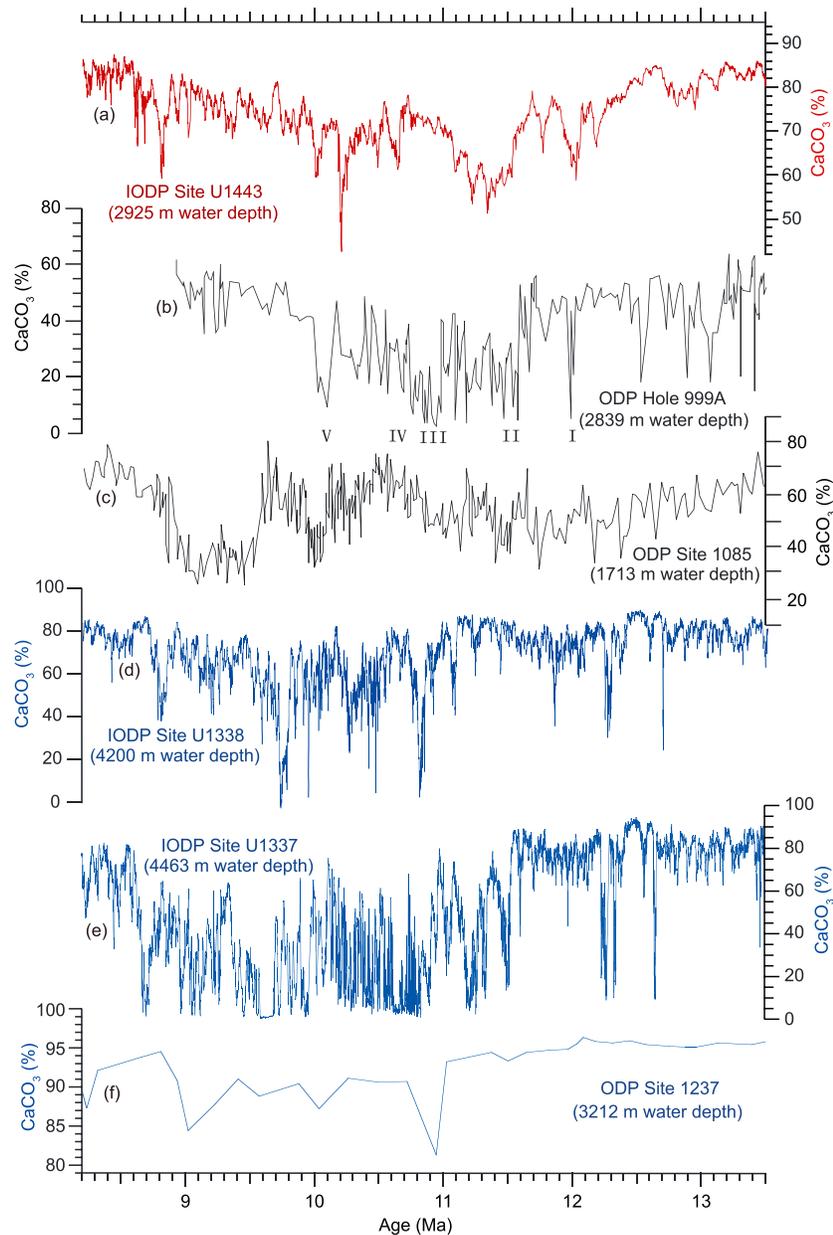
Figure 7. Comparison of carbonate content at ODP and IODP sites in the Indian, Atlantic, and Pacific Oceans. (a) Indian Ocean Site U1443; (b) Caribbean Sea Hole 999A (Roth et al., 2000); (c) southeastern Atlantic Site 1085 (Diester-Haass et al., 2004); (d) eastern equatorial Pacific Site U1338 (Lyle & Baldauf, 2015); (e) eastern equatorial Pacific Site U1337 (Shackford et al., 2014 on revised age model, see supporting information Figure S7); and (f) southeastern Pacific Site 1237 (Abe et al., 2006). IODP = International Ocean Discovery Program; ODP = Ocean Drilling Program.

occurs between 9 and 8.5 Ma (Figures 7 and 8), suggesting a common cause, such as a global change in climate or ocean biogeochemistry.

4.2. Multiple Causes of the Carbonate Crash in the Indian Ocean?
4.2.1. Ocean Carbonate Partitioning
Roth et al. (2000) suggested that an initial closure of the low-latitude deepwater connection between the Pacific and Atlantic Oceans led to an intensification of North Atlantic deep water production and a reorganization of Atlantic thermohaline overturning circulation that triggered the carbonate crash. Detailed biostratigraphic and paleobathymetric studies indicated a shallowing of the Central American Seaway from bathyal to neritic depths between 12.8 and 7.1 Ma (e.g., Coates et al., 2004), providing evidence for
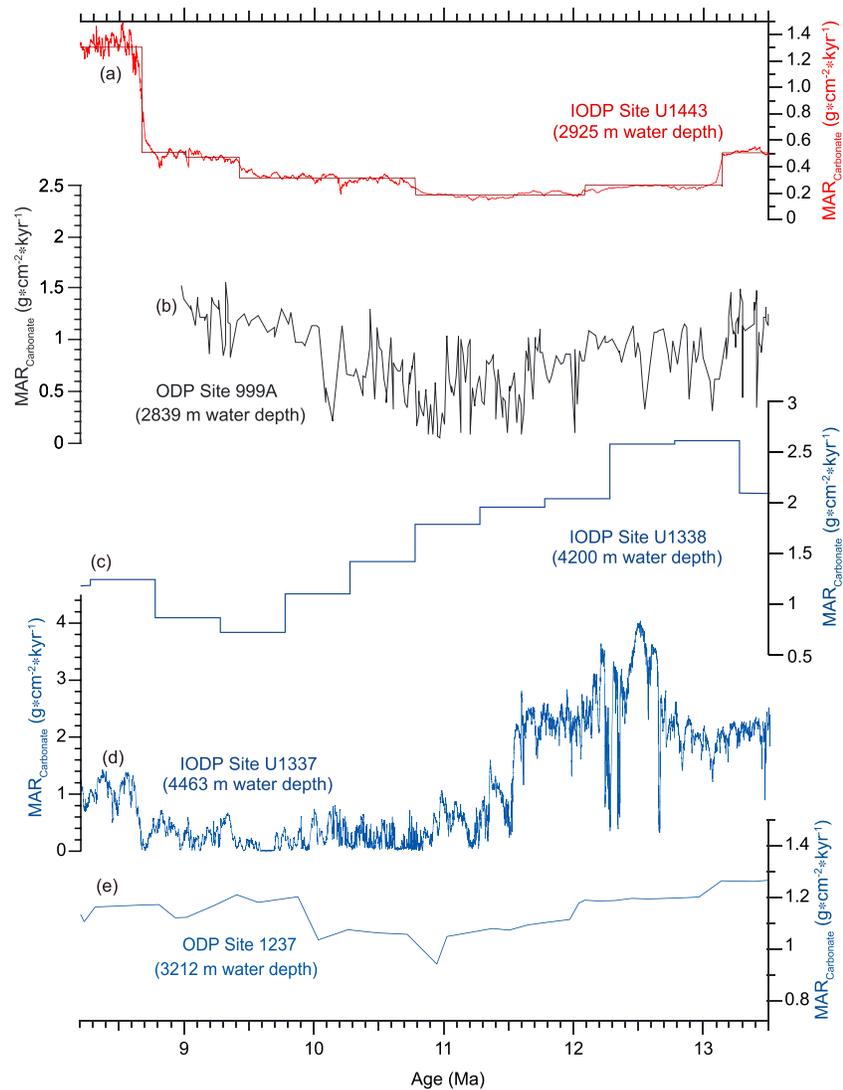
Figure 8. Comparison of carbonate MARs at ODP and IODP sites in the Indian, Atlantic, and Pacific Oceans. (a) Indian Ocean Site U1443; (b) Caribbean Sea Hole 999A (Roth et al., 2000); (c) eastern equatorial Pacific Site U1338 (Lyle & Baldauf, 2015); (d) eastern equatorial Pacific Site U1337 (Shackford et al., 2014 on revised age model, see supporting information Figure S7); and (e) southeastern Pacific Site 1237 (Abe et al., 2006). MAR at Site U1338 was calculated using average values for sedimentation rate and calcium carbonate concentration between age tie points. MAR at Sites 999A and 1237 is based on discrete measurements of calcium carbonate concentration. MAR at Site U1337 was calculated using the same method as for Site U1443. MAR calculated with average sedimentation rate between age tie points at Site U1443 is shown as black line. Note that vertical axes in Figure 8a and 8d have different scales than in Figures 8b–8d.
IODP = International Ocean Discovery Program; MAR = mass accumulation rate; ODP = Ocean Drilling Program.

sustained deepwater exchange between the Pacific and the Atlantic Oceans until at least 12.8 Ma. A link between the closure of this deepwater connection and the onset of intense carbonate dissolution events in the Caribbean at ~11.5 Ma is plausible but does not explain the earlier episodes of reduced carbonate accumulation in the Pacific and Indian Oceans (Figure 7). In addition, this scenario does not explain the relatively consistent termination of the carbonate crash in all tropical ocean basins between 9 and 8.5 Ma.

4.2.2. Changes in Ocean Circulation and Productivity

The onset of the carbonate crash in the Indian Ocean coincided with a global increase in benthic $\delta^{18}O$ (~0.5‰) between 13.2 and 13.0 Ma (the Mi4 glaciation of Miller et al., 1998), which probably relates to Antarctic ice sheet expansion and deepwater cooling (Figures 1 and 4). Roth et al. (2000) and Preiß-Daimler et al. (2013) suggested that high-latitude cooling was associated with increased formation of

corrosive southern sourced deep and intermediate water masses, which spread northward across the equator. However, it is puzzling that the earlier and more important Mi3 glaciation (Miller et al., 1998) and benthic δ^{18}O step (~1‰) between 13.9 and 13.8 Ma did not lead to a decrease in carbonate accumulation. Instead, this was associated with a substantial deepening of the CCD and increased carbonate preservation in the deep eastern equatorial Pacific Ocean (Holbourn et al., 2014; Lyle et al., 1995). Furthermore, the contrast between the major global increases in planktonic and benthic δ^{13}C during the carbon isotope maximum CM6 (~13.8–13.5 Ma) following Mi3 and the decreasing δ^{13}C trend between ~13.5 and 12.8 Ma following Mi4 (~13.5–12.8 Ma) implies fundamentally different responses of the ocean circulation and carbon cycle to these high-latitude cooling events.

The carbonate decline at the onset of the carbonate crash in the Indian Ocean may have been stimulated by a reorganization of ocean circulation and nutrient cycles associated with a change toward drier and cooler climate conditions, following the second pulse of ice sheet expansion and global cooling at 13.2–13.0 Ma. Cooling of deep and intermediate water masses originating from the Southern Hemisphere may have promoted steepening of the thermocline and increased stratification, thus, limiting nutrient cycling from intermediate waters into the photic zone. Changes in oxygen isotope and assemblage composition of shallow and deep dwelling planktic foraminifers at western equatorial Pacific Sites 289 (Gasperi & Kennett, 1993) and 806 (Nathan & Leckie, 2009) as well as in shallow water sites off southern Australia (Gallagher et al., 2001) support strengthening of vertical thermal gradients following Antarctic glaciation. In the Indian Ocean, this may have been exacerbated by a weakening of monsoonal circulation that inhibited mixing and contributed to a stratified upper ocean between 13 and 11 Ma. However, such changes cannot explain major decreases in carbonate flux to the deep-sea sediment reservoir over extended time periods on a global scale without balancing the budget either by increased carbonate deposition in shelf seas or a reduction of terrigenous calcium and carbonate flux into the ocean (Milliman, 1993).

4.2.3. Carbonate Budget: Changes in Carbonate Inventories During the Carbonate Crash

The low carbonate accumulation in vast areas of the tropical Pacific and Indian Oceans over the prolonged carbonate crash interval must have been compensated either by intensified carbonate accumulation in partitioned regions of the world's ocean (for instance, in shelf and marginal seas of the Paratethys/Atlantic and/or at higher latitudes) or by a decrease in the riverine flux of calcium and HCO_3^- (alkalinity) into the oceans. The HCO_3 concentration in rivers is mainly related to the balance of precipitation and evaporation in the drainage region, whereas the riverine HCO_3^- flux normalized to drainage area is closely correlated with the carbonate mineral content of river basins. Today, rivers in low (<30°), middle (30°–60°), and high (>60°) latitudes have an average HCO_3^- concentration of 0.584, 1.649, and 1.154 mM, respectively, and account for 42.6%, 47.3%, and 10.1% of the total global dissolved inorganic carbon flux to the ocean (Cai et al., 2008). Thus, midlatitude rivers carry a disproportionally high dissolved inorganic carbon flux in relation to a relatively small (26%) amount of freshwater discharge. In contrast, typical monsoonal low-latitude rivers, such as the Pearl River, are characterized by high carbonate mineral content and the highest chemical weathering rates in the warm and wet environments of their drainage basins. However, they have low HCO_3^- concentrations due to dilution by high precipitation in the watershed (Cai et al., 2008).

Climate cooling and the sea level fall associated with the middle Miocene expansion of the Antarctic ice sheet must have affected weathering patterns on land and the HCO_3^- flux of rivers in the Eurasian and American monsoonal areas. Global cooling would have led to a contraction of the tropical rainbelt and reduced HCO_3^- input from low-latitude rivers. In addition, there is evidence that a prolonged dry period prevailed between ~13 and 11 Ma at midlatitudes in Eurasia (Böhme et al., 2008; Jiang & Ding, 2008; Tang & Ding, 2013), which would have also decreased the input from midlatitude rivers with high HCO_3^- concentrations. The overall reduced calcium and alkalinity flux to the world's ocean would have led to decreased carbonate accumulation and increased organic carbon accumulation in the deep ocean. In turn, this would have contributed to a reduction in CO_2 release to the atmosphere, as during Pleistocene glacial intervals (Cartapanis et al., 2016, 2018).

4.3. Early Onset of the Biogenic Bloom in the Indian Ocean?

Following the carbonate crash, Neogene sedimentation patterns in the eastern equatorial Pacific show a distinct increase in biogenic accumulation that steepens with latitude toward the Equator (Farrell et al., 1995; Van Andel et al., 1975). This major increase in both carbonate and opal accumulation, termed the "biogenic

bloom", was later recognized at other upwelling locations in the Pacific Ocean, northwest Indian Ocean and perhaps southeast Atlantic Ocean within a rather broad and loosely defined interval between ~10 and ~3.8 Ma (Cortese et al., 2004; Dickens & Owen, 1999; Diester-Haass et al., 2004; Diester-Haass et al., 2006; Grant & Dickens, 2002; Gupta et al., 2004). In the eastern equatorial Pacific Ocean, Lyle and Baldauf (2015) identified the start and end of the biogenic bloom at 8 and 4.5 Ma with a maximum in opal and carbonate deposition between 7 and 6.4 Ma.

At Site U1443, sedimentation rates and biogenic carbonate MARs exhibit substantial increases at ~8.7 Ma, defining the end of the carbonate crash in the Indian Ocean. The rise in sedimentation rates at this site is primarily driven by an increase in carbonate MARs, although noncarbonate sediment accumulation rates also increase from $0.15 \, \mathrm{g \, cm^{-2} \, kyr^{-1}}$ (mean between 10.2 and 8.7 Ma) to $0.27 \, \mathrm{g \, cm^{-2} \, kyr^{-1}}$ after 8.7 Ma (supporting information Figure S3a). McNeill et al. (2017) identified a marked increase in sediment accumulation rates at ~9–9.5 Ma at Ninetyeast Ridge and Nicobar Fan sites, which these authors attributed to sediment rerouting within the Bengal-Nicobar Fan due to the interplay of tectonic, climatic (linked to monsoonal development), and sedimentological processes. The age discrepancy (~9–9.5 Ma vs. 8.7 Ma) for this prominent increase in sedimentation rates may be due to the lower resolution of shipboard age models used by McNeill et al. (2017).

An earlier increase in productivity in the western equatorial Indian Ocean was previously reported at 11 Ma by Smart et al. (2007). These authors attributed changes in benthic foraminiferal assemblages to local upwelling of cool nutrient-rich water masses. Low-resolution carbonate estimates in combination with a decline in benthic foraminiferal diversity and increase in high-productivity indicators additionally indicated a major shift towards a higher-productivity regime in the eastern equatorial Indian Ocean between 10 and 8 Ma (Gupta et al., 2004; Singh & Gupta, 2005). At Site U1443, the increase in Log (Ba/Ti) together with a shift of the sediment color from red to green after 11.2 Ma provides further evidence that primary production and organic carbon burial at the sea floor started to increase prior to the global onset of the biogenic bloom and remained elevated until at least 8.2 Ma. However, the short residence time of Ba (~10 kyr, Chan et al., 1976) requires excess Ba input into the ocean on a global scale to maintain elevated fluxes to the sea floor over timescales of several 100 kyr. Thus, either the increase in biogenic Ba was an intrinsic feature of the equatorial Indian Ocean and was balanced by decreased fluxes in other regions or riverine Ba and nutrient flux from land gradually increased after ~11 Ma. The Ba and sediment color records at Site U1443 further suggest that increased advection of nutrients from the Arabian Sea into the Ninetyeast Ridge region by summer monsoon driven currents may have already started by 11.2 Ma. Since then, summer monsoon wind forcing and upwelling in the Eastern Arabian Sea remain the dominant factors in controlling particle fluxes in the vicinity of Site U1443 (Unger et al., 2003).

5. Conclusion

This study provides a first detailed benthic isotope stratigraphy for the Indian Ocean over the interval 13.5 to 8.2 Ma and documents a prolonged episode of carbonate impoverishment in the equatorial Indian Ocean from ~13.2 to ~8.7 Ma, which we relate to the carbonate crash, originally identified in the eastern equatorial Pacific Ocean and the Caribbean Sea. The most intense phase of the carbonate crash, which lasted from ~11.5 to ~10 Ma, was synchronous in the Atlantic, Pacific, and Indian Oceans. Carbonate accumulation increased rapidly after ~8.7 Ma, marking the end of the carbonate crash in the Indian Ocean. At Site U1443, an increase in Log (Ba/Ti) together with a shift of the sediment color from red to green after 11.2 Ma provides evidence that primary production and organic carbon burial at the sea floor started to increase earlier in the Indian Ocean and prior to the global onset of the biogenic bloom.

Comparison of the timing and evolution of the carbonate crash in different ocean basins has a number of consequences for identifying the processes driving the carbonate crash: (1) The gradual and diachronous onset of the carbonate crash suggests that a global reorganization in ocean circulation driven by changes in ice volume or gateway configurations is an unlikely cause of the carbonate crash; (2) the global reduction in deep-sea carbonate deposition (~11.5 to 10 Ma) excludes interocean carbonate partitioning as the main cause for this event; (3) fundamental changes in the intensity of chemical weathering and riverine input of calcium and carbonate ions into the ocean reservoir must have been instrumental in driving the carbonate crash; and (4) an early increase in production and organic export flux at ~11.2 Ma in the Indian Ocean,

which predates the onset of the biogenic bloom in other regions, may have been linked to increased advection of nutrients into the Ninetyeast Ridge region and intensification of upper ocean mixing, associated with changes in the seasonality and intensity of Indian monsoonal wind and precipitation.

References

Archer, D. (1991). Modeling the calcite lysocline. *Journal of Geophysical Research*, *96*(C9), 17,037–17,050. https://doi.org/10.1029/91JC01812

Balsam, W. L., Deaton, B. C., & Damuth, J. E. (1999). Evaluating optical lightness as a proxy for carbonate content in marine sediment cores. *Marine Geology*, *161*(2-4), 141–153. https://doi.org/10.1016/S0025-3227(99)00037-7

Barron, J. A., Keller, G., & Dunn, D. A. (1985). A multiple microfossil biochronology for the Miocene. *Geological Society of America Memoirs*, *163*, 21–36. https://doi.org/10.1130/MEM163-p21

Berger, W. H., & Diester-Haass, L. (1988). Paleoproductivity: The benthic/planktonic ratio in foraminifera as a productivity index. *Marine Geology*, *81*(1-4), 15–25. https://doi.org/10.1016/0025-3227(88)90014-X

Berger, W. H., Leckie, R. M., Janecek, T. R., Stax, R., & Takayama, T. (1993). Neogene carbonate sedimentation on Ontong Java Plateau: Highlights and open questions. In T. R. Janacek, & W. V. Silter (Eds.), *Proceedings of the Ocean Drilling Program Scientific Results* (Vol. 130, pp. 711–744). College Station, TX: Ocean Drilling Program. https://doi.org/10.2973/odp.proc.sr.130.051.1993

Böhme, M., Ilg, A., & Winklhofer, M. (2008). Late Miocene "washhouse" climate in Europe. *Earth and Planetary Science Letters*, *275*(3-4), 393–401. https://doi.org/10.1016/j.epsl.2008.09.011

Boltovskoy, E., & Totah, V. I. (1992). Preservation index and preservation potential of some foraminiferal species. *Journal of Foraminiferal Research*, *22*(3), 267–273. https://doi.org/10.2113/gsjfr.22.3.267

Butzin, M., Lohmann, G., & Bickert, T. (2011). Miocene ocean circulation inferred from marine carbon cycle modeling combined with benthic isotope records. *Paleoceanography and Paleoclimatology*, *26*, PA1203. https://doi.org/10.1029/2009PA001901

Cai, W. -J., Guo, X., Chen, C. -T. A., Dai, M., Zhang, L., Zhai, W., et al. (2008). A comparative overview of weathering intensity and HCO₃⁻ flux in the world's major rivers with emphasis on the Changjiang, Huanghe, Zhujiang (Pearl) and Mississippi Rivers. *Continental Shelf Research*, *28*(12), 1538–1549. https://doi.org/10.1016/j.csr.2007.10.014

Cartapanis, O., Bianchi, D., Jaccard, S. L., & Galbraith, E. D. (2016). Global pulses of organic carbon burial in deep-sea sediments during glacial maxima. *Nature Communications*, *7*(1). https://doi.org/10.1038/ncomms10796

Cartapanis, O., Galbraith, E. D., Bianchi, D., & Jaccard, S. (2018). Carbon burial in deep-sea sediment and implications for oceanic inventories of carbon and alkalinity over the last glacial cycle. *Climate of the Past*, *14*(11), 1819–1850. https://doi.org/10.5194/cp-14-1819-2018

Chan, L. H., Edmond, J. M., Stallard, R. F., Broecker, W. S., Chung, Y. C., Weiss, R. F., & Ku, T. L. (1976). Radium and barium at GEOSECS stations in the Atlantic and Pacific. *Earth and Planetary Science Letters*, *32*, 258–267. https://doi.org/10.1016/0012-821X(76)90066-2

Clemens, S. C., Kuhnt, W., LeVay, L. J., Anand, P., Ando, T., Bartol, M., et al. (2016). Site U1443. In S. C. Clemens, W. Kuhnt, L. J. LeVay, & the Expedition 353 Scientists (Eds.), *Indian Monsoon Rainfall, Proceedings of the international ocean discovery program* (Vol. 353, pp. 1–41). College Station, TX: International Ocean Discovery Program. https://doi.org/10.14379/iodp.proc.353.103.2016

Clemens, S. C., Kuhnt, W., LeVay, L. J., & the Expedition 353 Scientists (2015). International ocean discovery program preliminary report 353: Indian Monsoon Rainfall, International Ocean Discovery Program Publications.

Coates, A. G., Collins, L. S., Aubry, M. P., & Berggren, W. A. (2004). The geology of the Darien, Panama, and the late Miocene-Pliocene collision of the Panama arc with northwestern South America. *Geological Society of America Bulletin*, *116*(11-12), 1327–1344. https://doi.org/10.1130/B25275.1

Cortese, G., Gersonde, R., Hillenbrand, C. –. D., & Kuhn, G. (2004). Opal sedimentation shifts in the World Ocean over the last 15 Myr. *Earth and Planetary Science Letters*, *116*(11-12), 1327–1344. https://doi.org/10.1130/B25275.1

Dickens, G. R., & Owen, R. M. (1999). The latest Miocene–early Pliocene biogenic bloom: A revised Indian Ocean perspective. *Marine Geology*, *161*(1), 75–91. https://doi.org/10.1016/S0025-3227(99)00057-2

Diester-Haass, L., Billups, K., & Emeis, K. C. (2006). Late Miocene carbon isotope records and marine biological productivity: Was there a (dusty) link? *Paleoceanography*, *21*, PA4216. https://doi.org/10.1029/2006PA001267

Diester-Haass, L., Meyers, P. A., & Bickert, T. (2004). Carbonate crash and biogenic bloom in the late Miocene: Evidence from ODP Sites 1085, 1086, and 1087 in the Cape Basin, southeast Atlantic Ocean. *Paleoceanography*, *19*, PA1007. https://doi.org/10.1029/2003PA000933

Dunne, J. P., Hales, B., & Toggweiler, J. R. (2012). Global calcite cycling constrained by sediment preservation controls. *Global Biogeochemical Cycles*, *26*, B3023. https://doi.org/10.1029/2010GB003935

Dymond, J., Suess, E., & Lyle, M. (1992). Barium in deep-sea sediment: A geochemical proxy for paleoproductivity. *Paleoceanography*, *7*(2), 163–181. https://doi.org/10.1029/92PA00181

Eagle, M., Paytan, A., Arrigo, K. R., van Dijken, G., & Murray, R. W. (2003). A comparison between excess barium and barite as indicators of carbon export. *Paleoceanography*, *18*(1), 1021. https://doi.org/10.1029/2002PA000793

Emerson, S., & Bender, M. (1981). Carbon fluxes at the sediment-water interface of the deep-sea: calcium carbonate preservation. *Journal of Marine Research*, *39*, 139–162.

Farrell, J. W., Raffi, I., Janecek, I., Murray, D. W., Levitan, I., Dadey, K. A., et al. (1995). Late Neogene sedimentation patterns in the eastern equatorial Pacific. In N. G. Pisias, L. A. Mayer, T. R. Janecek, A. Palmer-Julson & T. H. van Andel (Eds.), *Proceedings of the Ocean Drilling Program, Scientific Results*, (Vol. 138, pp. 717–756). College Station, TX: Ocean Drilling Program. https://doi.org/10.2973/odp.proc.sr.138.143.1995

Gallagher, S. J., Smith, A. J., Jonasson, K., Wallace, M. W., Holdgate, G. R., Daniels, J., & Taylor, D. (2001). The Miocene palaeoenvironmental and palaeoceanographic evolution of the Gippsland Basin, Southeast Australia: A record of Southern Ocean change. *Palaeogeography, Palaeoclimatology, Palaeoecology*, *172*(1-2), 53–80. https://doi.org/10.1016/S0031-0182(01)00271-1

Gasperi, J. T., & Kennett, J. P. (1993). Vertical thermal structure evolution of Miocene surface waters: Western equatorial Pacific DSDP Site 289. *Marine Micropaleontology*, *22*(3), 235–254. https://doi.org/10.1016/0377-8398(93)90046-Z

Gauns, M., Madhupratap, M., Ramaiah, N., Jyothibabu, R., Fernandes, V., Paul, J. T., & Prasanna Kumar, S. (2005). Comparative accounts of biological productivity characteristics and estimates of carbon fluxes in the Arabian Sea and the Bay of Bengal. *Deep Sea Research. Part II, Topical Studies in Oceanography*, *52*(14-15), 2003–2017. https://doi.org/10.1016/j.dsr2.2005.05.009

Giosan, L., Flood, R. D., & Aller, R. C. (2002). Paleoceanographic significance of sediment color on western North Atlantic drifts: I. Origin of color. *Marine Geology*, *189*, 25–41. https://doi.org/10.1016/S0025-3227(02)00321-3

Glasby, G. P. (1991). Mineralogy, geochemistry, and origin of Pacific red clays: A review. *New Zealand Journal of Geology and Geophysics*, *34*, 167–176. https://doi.org/10.1080/00288306.1991.9514454

Goldberg, E. D., & Arrhenius, G. O. S. (1958). Chemistry of Pacific pelagic sediments. *Geochimica et Cosmochimica Acta*, *13*(2), 153–212. https://doi.org/10.1016/0016-7037(58)90046-2

Gordon, A. L., Shroyer, E. L., Mahadevan, A., Sengupta, D., & Freilich, M. (2016). Bay of Bengal: 2013 northeast monsoon upper-ocean circulation. *Oceanography*, *29*(2), 82–91. https://doi.org/10.5670/oceanog.2016.41

Goswami, B. N., Rao, S. A., Sengupta, D., & Chakravorty, S. (2016). Monsoons to mixing in the Bay of Bengal: Multiscale air-sea interactions and monsoon predictability. *Oceanography*, *29*(2), 18–27. https://doi.org/10.5670/oceanog.2016.35

Gradstein, F. M., Ogg, J. G., Schmitz, M. D., & Ogg, G. M. (2012). *The geologic time scale 2012*. Amsterdam: Elsevier.

Grant, K. M., & Dickens, G. R. (2002). Coupled productivity and carbon isotope records in the southwest Pacific Ocean during the late Miocene–early Pliocene biogenic bloom. *Palaeogeography, Palaeoclimatology, Palaeoecology*, *187*(1), 61–82. https://doi.org/10.1016/S0031-0182(02)00508-4

Gupta, A. K., Singh, R. K., Sudheer, J., & Thomas, E. (2004). Indian Ocean high-productivity event (10–8 Ma): Linked to global cooling or to the initiation of the Indian monsoons? *Geology*, *32*(9), 753–756. https://doi.org/10.1130/G20662.1

Hendy, I. L. (2010). Diagenetic behavior of barite in a coastal upwelling setting. *Paleoceanography and Paleoclimatology*, *25*, PA4103. https://doi.org/10.1029/2009PA001890

Holbourn, A., Kuhnt, W., Lyle, M., Schneider, L., Romero, O. E., & Andersen, N. (2014). Middle Miocene climate cooling linked to intensification of eastern equatorial Pacific upwelling. *Geology*, *42*(1), 19–22. https://doi.org/10.1130/G34890.1

Holbourn, A. E., Kuhnt, W., Clemens, S., Kochhann, K., Jöhnck, J., Lübbers, J., & Andersen, N. (2018). Late Miocene climate cooling and intensification of southeast Asian winter monsoon. *Nature Communication*, *9*(1), 1584. https://doi.org/10.1038/s41467-018-03950-1

Holbourn, A. E., Kuhnt, W., Clemens, S., Prell, W., & Andersen, N. (2013). Middle to late Miocene stepwise climate cooling: Evidence from a high-resolution deep water isotope curve spanning 8 million years. *Paleoceanography*, *28*, 688–699. https://doi.org/10.1002/2013PA002538

Horner, T. J., Pryer, H. V., Nielsen, S. G., Crockford, P. W., Gauglitz, J. M., Wing, B. A., & Ricketts, R. D. (2017). Pelagic barite precipitation at micromolar ambient sulfate. *Nature Communications*, *8*(1), 1342. https://doi.org/10.1038/s41467-017-01229-5

Ittekkot, V., Nair, R. R., Honjo, S., Ramaswamy, V., Bartsch, M., Manganini, S., & Desai, B. N. (1991). Enhanced particle fluxes in Bay of Bengal induced by injection of fresh water. *Nature*, *351*(6325), 385–387. https://doi.org/10.1038/351385a0

Iversen, M. H., & Ploug, H. (2010). Ballast minerals and the sinking carbon flux in the ocean: Carbon-specific respiration rates and sinking velocity of marine snow aggregates. *Biogeosciences*, *7*(9), 2613–2624. https://doi.org/10.5194/bg-7-2613-2010

Jiang, H. C., & Ding, Z. L. (2008). A 20 Ma pollen record of East-Asian summer monsoon evolution from Guyuan, Ningxia, China. *Palaeogeography, Palaeoclimatology, Palaeoecology*, *265*(1-2), 30–38. https://doi.org/10.1016/j.palaeo.2008.04.016

Jiang, S., Wise, S. W., Wang, Y., & Teagle, D. A. H. (2007). Cause of the middle/late Miocene carbonate crash: Dissolution or low productivity. In D. A. H. Teagle, D. S. Wilson, G. D. Acton, & D. A. Vanko (Eds.), *Proceedings of the Ocean Drilling Program, Scientific Results* (Vol. 206, pp. 1–24). College Station, Texas: Ocean Drilling Program. https://doi.org/10.2973/odp.proc.sr.206.013.2007

Keller, G., & Barron, J. A. (1983). Paleoceanographic implications of Miocene deep-sea hiatuses. *Geological Society of America Bulletin*, *94*(5), 590–613. https://doi.org/10.1130/0016-7606(1983)94%3C590:PIOMDH%3E2.0.CO;2

Klaas, C., & Archer, D. E. (2002). Association of sinking organic matter with various types of mineral ballast in the deep sea: Implications for the rain ratio. *Global Biogeochemical Cycles*, *16*(4), 1116. https://doi.org/10.1029/2001GB001765

König, I., Drodt, M., Suess, E., & Trautwein, A. X. (1997). Iron reduction through the tan-green color transition in deep-sea sediments. *Geochimica et Cosmochimica Acta*, *61*(8), 1679–1683. https://doi.org/10.1016/S0016-7037(97)00007-0

Kuhnt, W., Holbourn, A., Hall, R., Zuvela, M., & Käse, R. (2004). Neogene history of the Indonesian throughflow. *Continent-Ocean Interactions within East Asian Marginal Seas, Geophysical Monograph*, *149*, 299–320. https://doi.org/10.1029/149GM16

Le Moigne, F. A. C., Gallinari, M., Laurenceau, E., & De La Rocha, C. L. (2013). Enhanced rates of particulate organic matter remineralization by microzooplankton are diminished by added ballast minerals. *Biogeosciences*, *10*(9), 5755–5765. https://doi.org/10.5194/bg-10-5755-2013

Lutz, M., Dunbar, R., & Caldeira, K. (2002). Regional variability in the vertical flux of particulate organic carbon in the ocean interior. *Global Biogeochemical Cycles*, *16*(3), 1037. https://doi.org/10.1029/2000GB001383

Lyle, M. (1983). The brown-green color transition in marine sediments: A marker of the Fe (III) - Fe (II) redox boundary. *Limnology and Oceanography*, *28*(5), 1026–1033. https://doi.org/10.4319/lo.1983.28.5.1026

Lyle, M., & Backman, J. (2013). Data report: Calibration of XRF-estimated CaCO₃ along the Site U1338 splice. In H. Pälike, M. Lyle, H. Nishi, I. Raffi, K. Gamage, A. Klaus, & the Expedition 320/321 Scientists (Eds.), *Proceedings of the Integrated Ocean Drilling Program* (Vol. 320, pp. 1–16). Tokyo: (Integrated Ocean Drilling Program Management), International, Inc. https://doi.org/10.2204/iodp.proc.320321.205.2013

Lyle, M., & Baldauf, J. (2015). Biogenic sediment regimes in the Neogene equatorial Pacific, IODP Site U1338: Burial, production, and diatom community. *Palaeogeography, Palaeoclimatology, Palaeoecology*, *433*, 106–128. https://doi.org/10.1016/j.palaeo.2015.04.001

Lyle, M., Dadey, K. A., & Farrell, J. W. (1995). The Late Miocene (11-8 Ma) Eastern Pacific Carbonate Crash: evidence for reorganization of deep-water Circulation by the closure of the Panama Gateway. In N. G. Pisias, L. A. Mayer, T. R. Janecek, A. Palmer-Julson & T. H. van Andel (Eds.), *Proceedings of the Ocean Drilling Program* (Vol. 138, pp. 821–838). College Station, TX: Ocean Drilling Program. https://doi.org/10.2973/odp.proc.sr.138.157.1995

Mayer, L. A., Shipley, T. H., & Winterer, E. L. (1986). Equatorial Pacific seismic reflectors as indicators of global oceanographic events. *Science*, *233*(4765), 761–764. https://doi.org/10.1126/science.233.4765.761

Mayer, L. A., Theyer, F., Barron, J. A., Dunn, D. A. , Handyside, T., Hills, S., et al. (1985). *Initial reports of the deep sea drilling project* (Vol. 85, p. 1021). Washington: U.S. Government Printing. https://doi.org/10.2973/dsdp.proc.85.1985

McNeill, L. C., Dugan, B., Backman, J., Pickering, K. T., Pouderoux, H. F., Henstock, T. J., et al. (2017). Understanding Himalayan erosion and the significance of the Nicobar Fan. *Earth and Planetary Science Letters*, *475*, 134–142. https://doi.org/10.1016/j.epsl.2017.07.019

Miller, K. G., Mountain, G. S., Browning, J. V., Kominz, M., Sugarman, P. J., Christie-Blick, N., & Katz, M. E. (1998). Cenozoic global sea level, sequences, and the New Jersey transect: Results from coastal plain and continental slope drilling. *Reviews of Geophysics*, *36*(4), 569–601. https://doi.org/10.1029/98RG01624

Milliman, J. D. (1993). Production and accumulation of calcium carbonate in the ocean: Budget of a nonsteady state. *Global Biogeochemical Cycles*, *7*(4), 927–957. https://doi.org/10.1029/93GB02524

Nathan, S. A., & Leckie, R. M. (2009). Early history of the Western Pacific Warm Pool during the middle to late Miocene (~13.2–5.8 Ma): Role of sea-level change and implications for equatorial circulation. *Palaeogeography, Palaeoclimatology, Palaeoecology*, *274*(3), 140–159. https://doi.org/10.1016/j.palaeo.2009.01.007

Nguyen, T. M. P., Petrizzo, M. R., & Speijer, R. P. (2009). Experimental dissolution of a fossil foraminiferal assemblage (Paleocene–Eocene Thermal Maximum, Dababiya, Egypt): Implications for paleoenvironmental reconstructions. *Marine Micropaleontology*, *73*, 241–258. https://doi.org/10.1016/j.marmicro.2009.10.005

Ogg, J. G. (2012). Geomagnetic polarity time scale. In F. M. Gradstein, J. G. Ogg, M. D. Schmitz, & G. M. Ogg (Eds.), *The geologic time scale 2012* (pp. 85–113). Amsterdam: Elsevier. https://doi.org/10.1016/B978-0-444-59425-9.00005-6

Paillard, D., Labeyrie, L., & Yiou, P. (1996). Macintosh program performs time-series analysis. *Eos, Transactions American Geophysical Union*, *77*(39), 379–379. https://doi.org/10.1029/96EO00259

Pälike, H., Lyle, M. W., Nishi, H., Raffi, I., Ridgwell, A., Gamage, K., et al. (2012). A Cenozoic record of the equatorial Pacific carbonate compensation depth. *Nature*, *488*(7413), 609–614. https://doi.org/10.1038/nature11360

Pälike, H., Nishi, H., Lyle, M., Raffi, I., Gamage, K., Klaus, A., & the Expedition 320/321 Scientists (2010). Expedition 320/321 summary. In H. Pälike, M. Lyle, H. Nishi, I. Raffi, K. Gamage, A. Klaus, & the Expedition 320/321 Scientists (Eds.), *Proceedings of the Integrated Ocean Drilling Program*, 320/321. (pp. 1–141). Tokyo: Integrated Ocean Drilling Program Management International, Inc. https://doi.org/10.2204/iodp.proc.320321.101.2010

Peterson, L. C., & Backman, J. (1990). Late Cenozoic carbonate accumulation and the history of the carbonate compensation depth in the western equatorial Indian Ocean. In R. A. Duncan, J. Backman, & L. C. Peterson (Eds.), *Proceedings of the Ocean Drilling Program, Scientific Results, Leg 115, Mascarene Plateau* (pp. 467–507). College Station: ODP, Texas A&M University. https://doi.org/10.2973/odp.proc.sr.115.163.1990

Peterson, L. C., Murray, D. W., Ehrmann, W. U., & Hempel, P. (1992). Cenozoic carbonate accumulation and compensation depth changes in the Indian Ocean. *Synthesis of results from scientific drilling in the Indian Ocean*, *70*, 311–333. https://doi.org/10.1029/GM070p0311

Piela, C., Lyle, M., Marcantonio, F., Baldauf, J. G., & Olivarez, A. (2012). Biogenic sedimentation in the equatorial Pacific: Carbon cycling and paleoproduction, 12–24 Ma. *Paleoceanography*, *27*, PA2204. https://doi.org/10.1029/2011PA002236

Preiß-Daimler, I. V., Henrich, R., & Bickert, T. (2013). The final Miocene carbonate crash in the Atlantic: Assessing carbonate accumulation, preservation and production. *Marine Geology*, *343*, 39–46. http://doi.org/10.1016/j.margeo.2013.06.010

Roth, J. M., Droxler, A. W., & Kameo, K. (2000). The Caribbean carbonate crash at the middle to late Miocene transition: Linkage to the establishment of the modern global ocean conveyor. In R. M. Leckie, H. Sigurdsson, G. D. Acton, & G. Draper (Eds.), *Proceedings of the Ocean Drilling Program, Scientific Results* (Vol. 165, pp. 249–273). College Station, TX: Ocean Drilling Program. https://doi.org/10.2973/odp.proc.sr.165.013.2000

Shackford, J. K., Lyle, M., Wilkens, R., & Tian, J. (2014). Data report: Raw and normalized elemental data along the Site U1335, U1336, and U1337 splices from X-ray fluorescence scanning. In H. Pälike, M. Lyle, H. Nishi, I. Raffi, K. Gamage, A. Klaus, & the Expedition 320/321 Scientists (Eds.), *Proceedings of the Integrated Ocean Drilling Program*, 320/321. (pp. 1–17). Tokyo: Integrated Ocean Drilling Program Management International, Inc. https://doi.org/10.2204/iodp.proc.320321.216.2014

Singh, R. K., & Gupta, A. K. (2005). Systematic decline in benthic foraminiferal species diversity linked to productivity increases over the last 26 Ma in the Indian Ocean. *Journal of Foraminiferal Research*, *35*(3), 219–227. https://dx.doi.org/10.2113/35.3.219

Smart, C. W., Thomas, E., & Ramsay, A. T. (2007). Middle–late Miocene benthic foraminifera in a western equatorial Indian Ocean depth transect: Paleoceanographic implications. *Palaeogeography, Palaeoclimatology, Palaeoecology*, *247*(3-4), 402–420. https://doi.org/10.1016/j.palaeo.2006.11.003

Tang, Z. -H., & Ding, Z. -L. (2013). A palynological insight into the Miocene aridification in the Eurasian interior. *Palaeoworld*, *22*, 77–85. https://doi.org/10.1016/j.palwor.2013.05.001

Theyer, F., Mayer, L. A., Barron, J. A., & Thomas, E. (1985). The equatorial Pacific high-productivity belt: Elements for a synthesis of Deep Sea Drilling Project Leg 85 results. In L. Mayer, F. Theyer, & E. Thomas (Eds.), *Initial Report, Deep Sea Drilling Project* (Vol. 85, pp. 971–985). Washington: U.S. Government Printing Office. https://doi.org/10.2973/dsdp.proc.85.133.1985

Thunnell, R. C. (1976). Optimum indices of calcium carbonate dissolution in deep-sea sediments. *Geology*, *4*(9), 525–528. https://doi.org/10.1130/0091-7613(1976)4%3C525:OIOCCD%3E2.0.CO;2

Tomczak, M., & Godfrey, J. S. (2003). Regional oceanography: An introduction. *Daya, Delhi*, *2*(1), 4–2.

Torres, M. E., Brumsack, H. J., Bohrmann, G., & Emeis, K. C. (1996). Barite fronts in continental margin sediments: A new look at barium remobilization in the zone of sulfate reduction and formation of heavy barites in diagenetic fronts. *Chemical Geology*, *127*(1–3), 125–139. https://doi.org/10.1016/0009-2541(95)00090-9

Unger, D., Ittekkot, V., Schäfer, P., Tiemann, J., & Reschke, S. (2003). Seasonality and interannual variability of particle fluxes to the deep Bay of Bengal: Influence of riverine input and oceanographic processes. *Deep-Sea Research II*, *50*(5), 897–923. https://doi.org/10.1016/S0967-0645(02)00612-4

Unger, D., & Jennerjahn, T. (2009). Impact of regional Indian Ocean characteristics on the biogeochemical variability of settling particles. *Indian Ocean Biogeochemical Processes and Ecological Variability*, *185*, 257–280. https://doi.org/10.1029/2008GM000703

Van Andel, T. H., Heath, G. R., & Moore, T. C. (1975). *Cenozoic history and paleoceanography of the central equatorial Pacific Ocean: A regional synthesis of Deep Sea Drilling Project data* (Vol. 143, pp. 1–134). Boulder, Colorado: Geological Society of America. https://doi.org/10.1130/MEM143-p1

Van der Zwaan, G. J., Jorissen, F. J., & de Stigter, H. C. (1990). The depth dependency of planktonic/benthic foraminiferal ratios: Constraints and applications. *Marine Geology*, *95*(1), 1–16. https://doi.org/10.1016/0025-3227(90)90016-D

Verardo, D. J., Froelich, P. N., & McIntyre, A. (1990). Determination of organic carbon and nitrogen in marine sediments using the Carlo Erba NA-1500 Analyzer. *Deep-Sea Research*, *37*(1), 157–165. https://doi.org/10.1016/0198-0149(90)90034-S

Von Breymann, M. T., Emeis, K. C., & Suess, E. (1992). Water depth and diagenetic constraints on the use of barium as a paleoproductivity indicator. In C. P. Summerhayes, W. L. Prell, & K. C. Emeis (Eds.), *Upwelling Systems: Evolution Since the Early Miocene, Geological Society Special Publication* (Vol. 64, pp. 273–284). London: Geological Society Special Publication.

Weltje, G. J., & Tjallingii, R. (2008). Calibration of XRF core scanners for quantitative geochemical logging of sediment cores: theory and application. *Earth and Planetary Science Letters*, *274*(3-4), 423–438. https://doi.org/10.1016/j.epsl.2008.07.054

References From the Supporting Information

Abe, C., Yamamoto, M., & Irino, T. (2006). Data report: Organic carbon and biomarker variations, Sites 1237 and 1239. In R. Tiedemann, A. C. Mix, C. Richter, & W. F. Ruddiman (Eds.), *Proceedings of the Ocean Drilling Program, Scientific Results* (Vol. 202, pp. 1–14). College Station, TX: Ocean Drilling Program. https://doi.org/10.2973/odp.proc.sr.202.203.2006

Bé, A. W. H., Morse, J. W., & Harrison, S. M. (1975). Progressive dissolution and ultrastructural breakdown of planktonic foraminifera. In W. V. Sliter, A. W. H. Bé, & W. H. Berger (Eds.), *Dissolution of Deep Sea Carbonates, Cushman Foundation Foraminifera Research Special Publications* (Vol. 13, pp. 27–55). Ithaka, NY: Cushman Foundation for Foraminiferal Research Special Publications (Journal of Foraminiferal Research).

Berggren, W. A., Kent, D. V., Swisher, C. C. III, & Aubry, M. -P. (1995). A revised Cenozoic geochronology and chronostratigraphy. In W. A. Berggren, D. V. Kent, M. P. Aubry, & J. Hardenbol (Eds.), *Geochronology, Time Scales and Global Stratigraphic Correlatio, Special Publication—SEPM* (Vol. 54, pp. 129–212). Tulsa, OK: Special Publication SEPM Society for Sedimentary Geology. https://doi.org/10.2110/pec.95.04.0129

Cande, S. C., & Kent, D. V. (1995). Revised calibration of the geomagnetic polarity timescale for the Late Cretaceous and Cenozoic. *Journal of Geophysical Research*, *100*(B4), 6093–6095. https://doi.org/10.1029/94JB03098

Chen, H. F., Yeh, P. -Y., Song, S. -R., Hsu, S. -C., Yang, T. -N., Wang, Y., et al. (2013). The Ti/Al molar ratio as a new proxy for tracing sediment transportation processes and its application in aeolian events and sea level change in East Asia. *Journal of Asian Earth Sciences*, *73*, 31–38. https://doi.org/10.1016/j.jseaes.2013.04.017

Gradstein, F. M., Ogg, J. G., & Smith, A. G. (2004). *A geologic time scale 2004* (Vol. 589). Cambridge: Cambridge University Press.

Hilgen, F., Lourens, L., & Van Dam, J. (2012). The Neogene Period. In F. M. Gradstein, J. G. Ogg, M. D. Schmitz, & G. M. Ogg (Eds.), *The geologic time scale 2012* (pp. 923–978). Amsterdam: Elsevier. https://doi.org/10.1016/B978-0-444-59425-9.00029-9

Holbourn, A., Kuhnt, W., Regenberg, M., Schulz, M., Mix, A., & Andersen, N. (2010). Does Antarctic glaciation force migration of the tropical rain belt? *Geology*, *38*(9), 783–786. https://doi.org/10.1130/G31043.1

Holbourn, A., Kuhnt, W., Schulz, M., Flores, J. A., & Andersen, N. (2007). Orbitally-paced climate evolution during the middle Miocene "Monterey" carbon-isotope excursion. *Earth and Planetary Science Letters*, *261*(3), 534–550. https://doi.org/10.1016/j.epsl.2007.07.026

Laskar, J., Fienga, A., Gastineau, M., & Manche, H. (2011). La2010: A new orbital solution for the long-term motion of the Earth. *Astronomy and Astrophysics*, *532*, A89. https://doi.org/10.1051/0004-6361/201116836

Laskar, J., Robutel, P., Joutel, F., Gastineau, M., Correia, A. C. M., & Levrard, B. (2004). A long-term numerical solution for the insolation quantities of the Earth. *Astronomy and Astrophysics*, *428*(1), 261–285. https://doi.org/10.1051/0004-6361:20041335

Mix, A. C., Tiedemann, R., Blum, P., Abrantes, F. F., Benway, H., & Cacho-Lascorz, I. (2003). *Proceedings of the ocean drilling program, Initial reports* (Vol. 202, pp. 1–107). College Station, Texas: Ocean Drilling Program. https://doi.org/10.2973/odp.proc.ir.202.108.2003

Raffi, I., & Flores, J. -A. (1995). Pleistocene through Miocene calcareous nannofossils from eastern equatorial Pacific Ocean. In N. G. Pisias, L. A. Mayer, T. R. Janecek, A. Palmer-Julson, & T. H. van Andel (Eds.), *Proceedings of the Ocean Drilling Program, Scientific Results* (Vol. 138, pp. 233–286). College Station, TX: Ocean Drilling Program. https://doi.org/10.2973/odp.proc.sr.138.112.1995

Sigurdsson, H., Leckie, R. M., Acton, G. D., Abrams, L. J., Bralower, T. J., & Carey, S. N. (1997). *Proceedings of the ocean drilling program, Initial reports* (Vol. 165, pp. 131–230). College Station, Texas: Ocean Drilling Program. https://doi.org/10.2973/odp.proc.ir.165.104.1997

Tian, J., Ma, X., Zhou, J., Jiang, X., Lyle, M., Shackford, J., & Wilkens, R. (2018). Paleoceanography of the east equatorial Pacific over the past 16 Myr and Pacific-Atlantic comparison: High resolution benthic foraminiferal δ^{18}O and δ^{13}C records at IODP Site U1337. *Earth and Planetary Science Letters*, *499*, 185–196. https://doi.org/10.1016/j.epsl.2018.07.025

Westerhold, T., Bickert, T., & Röhl, U. (2005). Middle to late Miocene oxygen isotope stratigraphy of ODP Site 1085 (SE Atlantic): New constrains on Miocene climate variability and sea-level fluctuations. *Palaeogeography, Palaeoclimatology, Palaeoecology*, *217*(3), 205–222. https://doi.org/10.1016/j.palaeo.2004.12.001